Journal of Controlled Release 140 (2009) 306–311

Contents lists available at ScienceDirect

Journal of Controlled Release

journal homepage: www.elsevier.com/locate/jconrel

Enhanced magnetic resonance imaging of experimental pancreatic tumor *in vivo* by block copolymer-coated magnetite nanoparticles with TGF-β inhibitor

Michiaki Kumagai [a,e,1], Mitsunobu R. Kano [b,f,1], Yasuyuki Morishita [b], Motomi Ota [a], Yutaka Imai [a], Nobuhiro Nishiyama [a,e,f], Masaki Sekino [c], Shoogo Ueno [d], Kohei Miyazono [b,f], Kazunori Kataoka [a,e,f,*]

[a] Department of Materials Engineering, Graduate School of Engineering, The University of Tokyo, 7-3-1 Hongo, Bunkyo-ku, Tokyo 113-8656, Japan
[b] Department of Molecular Pathology, Graduate School of Medicine, The University of Tokyo, 7-3-1 Hongo, Bunkyo-ku Tokyo 113-0033, Japan
[c] Department of Advanced Energy, Graduate School of Frontier Sciences, The University of Tokyo, 5-1-5, Kashiwanoha, Kashiwa-shi, Chiba, 277-8561, Japan
[d] Department of Applied Quantum Physics, Graduate School of Engineering, Kyushu University, 6-10-1 Hakozaki, Higashi-ku Fukuoka 812-8581, Japan
[e] Center for Disease Biology and Integrative Medicine, School of Medicine, The University of Tokyo, 7-3-1 Hongo, Bunkyo-ku, Tokyo 113-0033, Japan
[f] Center for NanoBio Integration, The University of Tokyo, 7-3-1 Hongo, Bunkyo-ku, Tokyo 113-8656, Japan

ARTICLE INFO

Article history:
Received 13 March 2009
Accepted 5 June 2009
Available online 12 June 2009

Keyword:
Magnetic resonance imaging
Pancreatic cancer
TGF-β
Magnetite nanoparticles
Poly(ethylene glycol)

ABSTRACT

Early detection of solid tumors, particularly pancreatic cancer, is of substantial importance in clinics. Enhanced magnetic resonance imaging (MRI) with iron oxide nanoparticles is an available way to detect the cancer. The effective and selective accumulation of these nanoparticles in the tumor tissue is needed for improved imaging, and in this regard, their longevity in the blood circulation time is crucial. We developed here block copolymer-coated magnetite nanoparticles for pancreatic cancer imaging, by means of a chelation between the carboxylic acid groups in poly(ethylene glycol)–poly(aspartic acid) block copolymer (PEG–PAsp) and Fe on the surface of the iron oxide nanoparticles. These nanoparticles had considerably narrow distribution, even upon increased ionic strength or in the presence of fetal bovine serum. The PEG–PAsp-coated nanoparticles were further shown to be potent as a contrast agent for enhanced MRI for an experimental pancreatic cancer, xenografts of the human-derived BxPC3 cell line in BALB/c nude mice, with combined administration of TGF-β inhibitor. Iron staining of tumor tissue confirmed the accumulation of the nanoparticles in tumor tissue. Use of the PEG–PAsp-coated magnetite nanoparticles, combined with the TGF-β inhibitor, is of promising clinical importance for the detection of intractable solid cancers, including pancreatic cancer.

1. Introduction

Pancreatic cancer, one of the intractable solid tumors, is the fourth leading cause of cancer-related deaths in the United States and the fifth in Japan [1]. The average survival period of patients suffering from advanced pancreatic adenocarcinoma is still extremely short, only 6 months, despite recent progress in the chemotherapies [2]. Although cancer detection and treatment have been greatly improved through the development of diagnostic imaging modalities, it is still difficult to detect pancreatic cancer [3]. Consequently, the development of diagnostic systems to detect these cancers is of great importance.

Recently, superparamagnetic iron oxide (SPIO) nanoparticles composed of either magnetite (Fe_3O_4) or maghemite (g-Fe_2O_3) have been studied as contrast agents for magnetic resonance (MR) imaging [4]. Commercial application for human diagnosis based on SPIO particles is currently available. However, since cancer detection requires the systemic administration of iron oxide nanoparticles, the circulation time of the particles must be prolonged. Several studies have already reported that the behavior of magnetic nanoparticles in the bloodstream depends closely on their nanoscale morphology, including overall diameter, size distribution, or nature of the surface [5,6]. Additionally, the surface modification of iron oxide nanoparticles has proved a versatile strategy for improving their biological performance, including the reduction of immunogenicity and enhancement of targeted delivery to specific tissues [7]. However, the overall correlation between the surface modification of nanoparticles and their *in vivo* behavior remains to be further elucidated.

Various methods of stabilization for SPIO nanoparticles have been reported to date [8]. One of the most feasible approaches could be the stabilization of SPIO by coated with biocompatible polymers [9]. Suitable polymers, including poly(ethylene glycol) (PEG) and its block copolymers, are promising for the development of SPIO systems with defined surface properties. This coating of particles with PEG, or PEGylation, to avoid their uptake by the reticuloendothelial system, is under intensive investigation. We also previously reported the accumulation of β-FeOOH nanoparticles coated with PEG–poly(α,β-aspartic acid) block copolymer

* Corresponding author. Department of Materials Engineering, Graduate School of Engineering, The University of Tokyo, 7-3-1 Hongo, Bunkyo-ku, Tokyo 113-8656, Japan.
E-mail address: kataoka@bmw.t.u-tokyo.ac.jp (K. Kataoka).
[1] Equal contribution.

0168-3659/$ – see front matter © 2009 Elsevier B.V. All rights reserved.
doi:10.1016/j.jconrel.2009.06.002

(PEG–PAsp) into experimental colon adenocarcinoma, which could be applicable for tumor-selective MR imaging [10]. The multivalent bonding of PEG-based block copolymer to magnetic nanoparticles may thus help to facilitate the accumulation of these nanoparticles into some solid tumors. However, magnetic nanoparticles of any design have not yet been successful in exhibiting sufficient accumulation in intractable solid cancers, including pancreatic adenocarcinoma [1]. In addition to improving the performance of iron-based contrast agents (e.g. biocompatibility), the co-administration of adjuvant small molecules could increase the accumulation of these agents in target cancer tissue. In fact, we have recently shown that the administration of the small molecule TGF-β inhibitor (LY364947) at a low dose [11], which could minimize the potential side effects of the TGF-β inhibitor, can alter the tumor microenvironment and enhance the EPR effect in these cancers [12]. Therefore, the combined use of TGF-β inhibitor could be promising to diagnose intractable cancers with a long-circulating MRI contrast agent. Here, we demonstrated the successful MR imaging of experimental pancreatic cancer by the systemic administration of newly developed SPIO nanoparticles coated by PEG–PAsp in aid of TGF-β inhibitor.

2. Materials and methods

2.1. Reagents

β-benzyl L-aspartate and bis(trichloromethyl)carbonate (triphosgene) were purchased from Sigma-Aldrich Corporation (St. Louis, MO, USA) and Tokyo Chemical Industry Co., Ltd. (Tokyo, Japan), respectively. α-Methoxy-ω-amino-poly(ethylene glycol) (CH_3O–PEG–NH_2; $M_w = 12000$) was purchased from NOF Corporation (Tokyo, Japan). Tetrahydrofuran (THF), *n*-hexane, *N,N*-dimethylformamide (DMF), CH_2Cl_2 were doubly-distilled according to the standard procedures. The magnetite nanoparticles were supplied by Toda Kogyo Corporation (Hiroshima, Japan; average particle size of magnetite: 10 nm). Resovist® was obtained from Bayer HealthCare Co., Ltd. (Osaka, Japan). TGF-β inhibitor was purchased from EMD Chemicals Inc. (San Diego, CA, USA) (LY364947; catalog no. 616451).

2.2. Synthesis of poly(ethylene glycol)–poly(α,β-aspartic acid) block copolymer (PEG–PAsp)

PEG–PAsp was synthesized by a previously reported procedure [13]. Briefly, poly (ethylene glycol)–*b*–poly(β-benzyl L-aspartate) block copolymer (PEG–PBLA) was prepared by ring-opening polymerization of N-carboxy anhydride of β-benzyl L-aspartate (BLA-NCA) from the ω-NH_2 group of PEG ($M_w = 1.2 \times 10^4$). Molecular weight distribution of PEG–PBLA was narrow as $M_w/M_n = 1.06$, which was determined by gel permeation chromatography [columns: TSK-gel G3000HHR, G4000HHR (Tosoh, Yamaguchi, Japan); eluent: DMF containing 10 mM LiCl; flow rate: 0.8 ml/min; detector: refractive index (RI); temperature: 40 °C]. The composition of these block copolymers was determined by ^{1}H NMR from peak intensity ratios of methylene protons of PEG (OCH_2CH_2: $d = 3.7$ ppm) and phenyl protons of the β-benzyl groups of PBLA ($-CH_2C_6H_5$: $d = 7.3$ ppm). The polymerization degree of BLA in block copolymer was calculated to be 38. The benzyl groups of PEG–PBLA were then removed by alkaline hydrolysis using 0.1 N NaOH to obtain PEG–PAsp as follows:

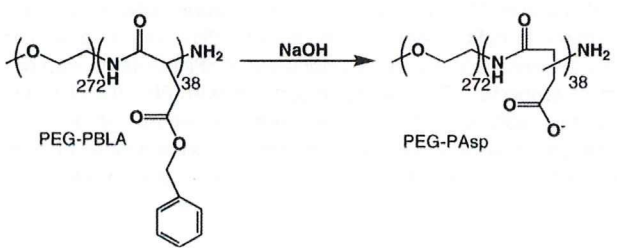

2.3. Preparation of PEG–PAsp-coated magnetite nanoparticles

PEG–PAsp-coated magnetite nanoparticles were prepared according to the previous method with slight modification [10]. Briefly, magnetite solution was quickly added to an aqueous solution of PEG–PAsp with varying feed molar ratios of aspartic acid residues to Fe ([Asp]/[Fe]) in the range of 0.01 to 1. The final concentration of magnetite was adjusted to 10 mmol/l. The mixed solutions were incubated at room temperature for 24 h to obtain magnetite nanoparticles coated with PEG–PAsp. Purification of the PEG–PAsp-coated magnetite nanoparticles was carried out by ultrafiltration (MWCO 200 000; polysulfone membrane, Toyo Roshi Co. Ltd., Tokyo, Japan).

2.4. Physicochemical characterization of the nanoparticles

The morphology and size distribution of the nanoparticles were examined by transmission electron microscopy (H-7000, Hitachi, Ltd., Tokyo, Japan) at an accelerating voltage of 75 kV. The TEM samples were prepared by mounting a drop of aqueous iron oxide nanoparticles suspension on carbon-coated 400 mesh Cu grids and allowing them to dry in air. Fourier transform infrared (FT-IR) spectra were obtained using a FT-IR spectrophotometer (FT/IR615, JASCO Corporation, Hachioji, Tokyo, Japan) with a resolution of 4 cm^{-1}. To characterize the interaction between block copolymer and magnetite nanoparticles, a small amount of nanoparticles powder was milled with KBr, and then pressed into a disc for analysis. Each spectrum was scanned 64 times to increase the signal-to-noise ratio. The Fe content in the nanoparticles was determined by ion coupled plasma-mass spectroscopy (ICP-MS, 4500, Hewlett Packard, Palo Alto, CA, USA). The amount of adsorbed block copolymer on magnetite nanoparticles was measured by thermogravimetric analysis (TGA) (EXSTAR6200 TG/DTA, Seiko Instruments Inc., Chiba, Japan) in nitrogen atmosphere with a heating rate of 10 °C/min in the temperature range of 25–1100 °C.

2.5. Light scattering and ζ-potential measurements

The size distribution of the PEG–PAsp-coated magnetite nanoparticles was examined by dynamic light scattering (DLS) DLS-7000 (Otsuka Electronics Co., Ltd., Osaka, Japan). Vertically polarized light with a wavelength of 488 nm from an Ar-ion laser (15 mW) was used as the incident beam. All measurements were conducted at 37 °C, and the data were analyzed by the cumulant method to determine the hydrodynamic diameters of the particles. The ζ-potential of PEG–PAsp-coated magnetite nanoparticles at 37 °C was measured by a Zetasizer NanoZS instrument equipped with a DTS5001 cell (Malvern Instruments Ltd., Worcestershire, UK).

2.6. Characterization of the r_2 relaxivities

The MR contrast effect of the magnetite nanoparticles was examined by measuring their proton relaxivities, r_2, of which the definition is the slope of the concentration dependence given as:

$$1/T_2 = 1/T_2(0) + r_2[\mathrm{Fe}]$$

Thus, a plot of $1/T_2$ versus concentration gives the relaxivity as the slope, where T_2 is the transversal relaxation time, $1/T_2$ is the transversal relaxation rate constant in the presence of a paramagnetic species, and $1/T_2(0)$ is the transversal relaxation rate constant in the absence of a paramagnetic species. The magnetite nanoparticles were dispersed into deionized water at concentrations of 0.5, 1.0, 1.5, 2.0, and 2.5 mM and the T_2 of these nanoparticle solutions was measured at 25 °C in water with a 0.47 T minispectrometer (Minispec, Bruker

Optics Inc., Woodlands, TX, USA) using the Carr–Purcell–Meiboom–Gill (CPMG) method [14].

2.7. In vivo MR imaging

The BxPC3 human pancreatic adenocarcinoma cell line was obtained from the American Type Culture Collection (Manassas, VA, USA). The BxPC3 cells were grown in RPMI 1640 medium supplemented with 10% FBS. BALB/c nude mice (female, 5–6 weeks of age), obtained from Charles River Laboratories Japan Inc. (Tokyo, Japan), were inoculated subcutaneously with BxPC3 cells (1×10^7 cells/mouse). After 3–4 weeks, MR imaging of the tumors was conducted with a 4.7 T scanner (INOVA200, Varian, Inc., Palo Alto, CA, USA). Twenty-four hours prior to the *in vivo* MR imaging, animals were treated with TGF-β inhibitor, 5 mg/ml in 4 μl of DMSO and diluted by 100 μl of PBS, at 1 mg/kg by intraperitoneal injection. Subsequently, the mice were injected at a dose of 0.1 mmolFe/kg, with Resovist® or PEG–PAsp-coated magnetite nanoparticles. A total of 4 conditions ($n=5$ mice each) were investigated, i.e. with or without TGF-β inhibitor for both Resovist® or PEG–PAsp-coated magnetite nanoparticles. Imaging was performed at different temporal points (e.g., preinjection, 1 h postinjection, and 2 h postinjection). For the T_2-weighted MR imaging of live mice, the following parameters were adopted: spin-echo method, point resolution = 234×234 μm, section thickness = 2.0 mm, TE = 60 ms, TR = 3000 ms, number of acquisitions = 5. All animals were treated in accordance with the guidelines of the Animal Ethics Committee of the University of Tokyo.

2.8. Histology

The excised samples were fixed overnight in 4% paraformaldehyde and then paraffin-embedded. Embedded samples were thin sliced at 10 μm thick and then stained using an Iron Stain Kit (Muto Pure Chemicals Co., Ltd., Tokyo, Japan), based on McFadzean's protocol [15], with nuclear post-staining by 1% Safranin O. Iron staining was observed using an AX80 microscope (Olympus Corporation, Tokyo, Japan). The photographs were further quantified using Adobe Photoshop software (Adobe Systems Incorporated, San Jose, CA, USA), ImageJ software (National Institute of Health, MD, USA), and Microsoft Excel software (Microsoft Corporation, Redmond, WA, USA).

3. Results and discussion

3.1. The physicochemical properties of the PEG–PAsp-coated magnetite nanoparticle: diameter and surface polymer density

For solid tumor diagnosis, it is important to develop well-designed magnetite nanoparticles. The key physicochemical properties of magnetite nanoparticles are size, surface polymer density, and surface charge, since these characteristics can affect accumulation of magnetite nanoparticles to solid tumor. The PEG–PAsp-coated magnetite nanoparticles were prepared by mixing solutions of magnetite nanoparticles and PEG–PAsp with various molar ratios of the Asp residues to Fe (Asp/Fe); Asp/Fe ranged from 0.01 to 0.5, where [Fe] = 10 mmol/l. As seen in Fig. 1, the transmission electron microscopy (TEM) image with 75 kV accelerating voltage of nanoparticles mounted on carbon grid from aqueous solution revealed that PEG–PAsp-coated magnetite nanoparticles take a cubic shape with a mean particle diameter of approximately 10 nm. The PEG–PAsp coating was observed as a layer with a thickness of approximately 5 nm, surrounding the magnetite nanoparticles. It was also observed in the TEM image that these PEG–PAsp-coated nanoparticles form clusters with a size range of 100 nm.

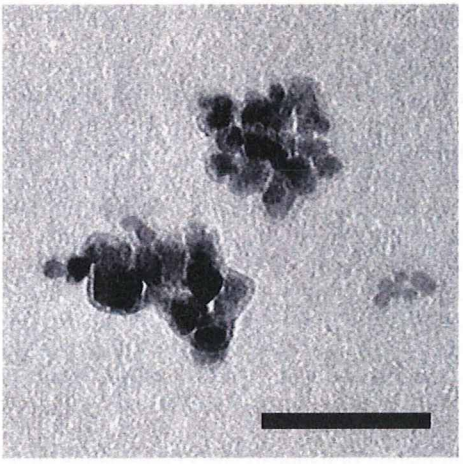

Fig. 1. TEM image of the PEG–PAsp-coated magnetite nanoparticles. Bar: 100 nm.

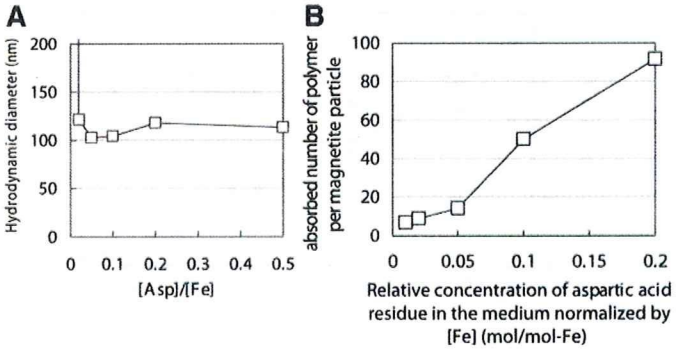

Fig. 2. Physicochemical properties of the PEG–PAsp-coated magnetite nanoparticles. (A) Hydrodynamic diameter vs. relative concentration of aspartic acid residue in the medium normalized by [Fe] (mol/mol-Fe) (=[Asp]/[Fe]), and (B) Change in the adsorbed density of PEG–PAsp on the magnetite surface estimated from TGA analysis with a bulk concentration of PEG–PAsp. Temperature = 37 °C; medium: distilled water.

The hydrodynamic diameter of these nanoparticles in aqueous medium was then measured with DLS and shown to be in the range of 100 to 120 nm with unimodal distribution, for Asp/Fe ratios ranging from 0.02–0.5. This DLS data is consistent with the cluster formation of nanoparticles indicated from TEM images. However, with a lowered Asp/Fe ratio as 0.01, the hydrodynamic diameter increased significantly (Fig. 2A). This result indicates that there is a critical surface concentration of PEG to effectively prevent the PEG–PAsp-coated magnetite nanoparticles from the agglomeration. The purified nanoparticles were stable in distilled water as 100 nm-scaled cluster at room temperature as well as at 37 °C, maintaining the initial photon count and distribution in DLS analysis for at least one month, even after the ultrafiltration to remove free PEG–PAsp possibly remained in the reactant.

The density of the PEG–PAsp block copolymer on the magnetite particle surface was estimated by TGA. Here, nanoparticles were heated in the nitrogen atmosphere to selectively vaporize the polymer fraction. Eventually, the amount of absorbed polymer on the surface of the nanoparticles was measured from the weight change by heating. The polymer density was then calculated from the TGA measurement for all the nanoparticles, assuming the cubic morphology as evidenced by microscopy and a density of 5.05 g/cm^3 for magnetite. As seen in Fig. 2B, the number of polymer strands on the nanoparticle surface was as high as 100. This data suggests that the PEG density on the magnetite nanoparticles is a little lower than that of PEGylated gold nanoparticles prepared through the surface tethering of PEG-SH [16].

3.2. The mechanism of PEG–PAsp adsorption on the magnetite nanoparticles

To confirm the formation of PEG–PAsp coating on the magnetite nanoparticles, the ζ-potential of bare and PEG–PAsp-coated magnetite nanoparticles was measured in 10 mM MOPS buffer as a function of

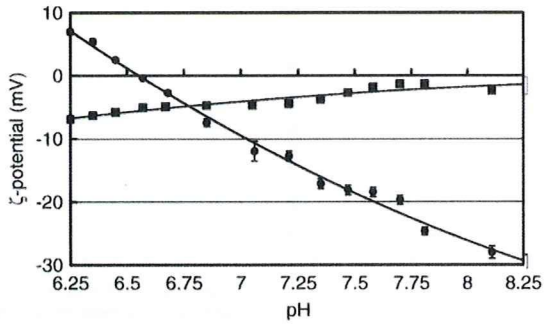

Fig. 3. Change in the ζ-potential with pH for bare (●) and PEG–PAsp-coated (■) magnetite nanoparticles. Temperature = 37 °C; medium: 10 mM MOPS buffer.

pH (Fig. 3). The isoelectric point (IEP) of the bare magnetite nanoparticles was estimated as approximately 6.6, which is consistent with the reported IEP value of iron oxide [17]. In a lower pH (below the IEP), the magnetite nanoparticle surface was protonated to result in a positive ζ-potential. Thus, in this pH range, electrostatic attraction between positively-charged magnetite nanoparticles and negatively charged PEG–PAsp is expected to occur, allowing the PEG–PAsp adsorption to the nanoparticle surface. Alternatively, the bare magnetite nanoparticles possess negative ζ-potential at physiological pH 7.4, whereas the ζ-potential shifted to the neutral value for PEG–PAsp modified nanoparticles in 10 mM MOPS buffer (pH 7.4), being consistent with the formation of a PEG shell layer. Also, these data suggest that there should be an adsorption mechanism other than simple electrostatic interaction, because magnetite has a negative ζ-potential value at pH 7.4 to induce electrostatic repulsive force against negatively charged carboxylates in PEG–PAsp. The adsorption mechanism under physiological pH was suggested to be the monodentate chelation (I) (Fig. 4) from the result of Fourier transform infrared spectroscopy [18], as explained in detail in Supplemental Text with Supplemental Fig. 1 and Supplemental Table 1.

3.3. Comparison study of the physicochemical characteristics of the PEG–PAsp- and dextran-coated magnetite nanoparticles

The MRI detection limit was compared between the PEG–PAsp- and dextran-coated magnetite nanoparticles in the field of 0.47 T at 25 °C from the relaxivity r_2, exhibiting the sensitivity of the T_2 MRI contrast agent. The dextran-coated magnetite used in this study was the one already in clinical use, Resovist®. Eventually, the relaxivity r_2 of the PEG–PAsp nanoparticle was calculated to be 138 $mM^{-1}\,s^{-1}$, the value similar to Resovist® [19].

The hydrodynamic diameter observed between the PEG–PAsp-coated and dextran-coated magnetite nanoparticles differed significantly in an NaCl-concentration-dependent manner (Fig. 5A). Although the hydrodynamic diameter of the PEG–PAsp-coated magnetite nanoparticles did not change significantly up to 3 M NaCl, indicating the appreciable stability of the PEG–PAsp-coating, that of Resovist® significantly increased even at NaCl = 0.15 M, and reached more than 1 μm at NaCl = 0.5 M, due to the drastic aggregation. Note that the PEG–PAsp-coated nanoparticles did not show any change in

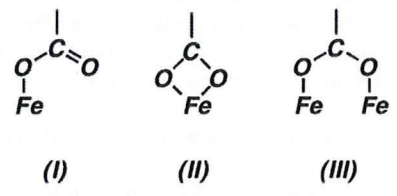

Fig. 4. Modes of carboxylate-metal complexation: monodentate (**I**), bidentate chelating (**II**), and bidentate bridging (**III**).

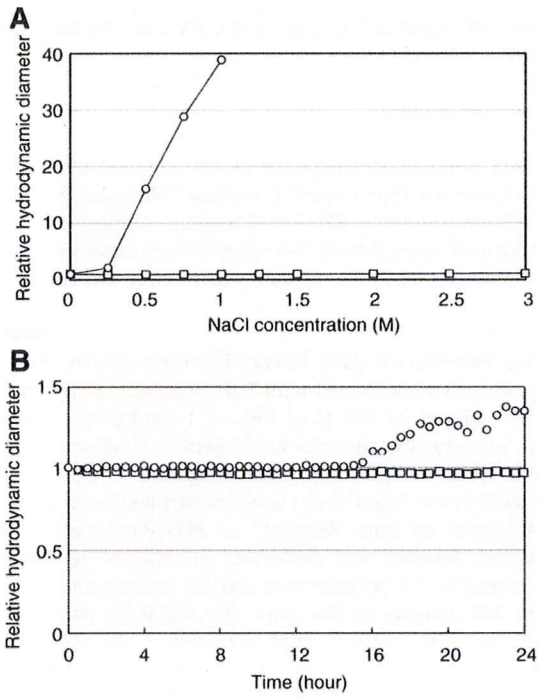

Fig. 5. NaCl concentration (A) and time (B) dependencies of the relative hydrodynamic diameter of magnetite nanoparticles, □: PEG–PAsp-coated nanoparticles, ○: dextran-coated nanoparticles (Resovist®). Fe concentration = 2 mmol/l; temperature = 37 °C; medium 10 mM Tris–HCl buffered saline (pH 7.4). 10% fetal bovine serum was contained in (B).

their size even after one month storage in 10 mM Tris–HCl buffered saline (pH 7.4, 37 °C) (data not shown).

The colloidal stability of the PEG–PAsp-coated magnetite nanoparticles in physiological conditions was also examined. We incubated them in 10 mM Tris–HCl buffered saline (pH 7.4) containing 10% fetal bovine serum at 37 °C for 24 h and measured the change of the hydrodynamic diameter (Fig. 5B). The size of the PEG–PAsp-coated magnetite nanoparticles did not obviously change during the 24-hour storage time. On the other hand, the size of Resovist® increased by the formation of aggregates after 16 h of storage time.

The stability of the PEG–PAsp-coated nanoparticles may come from the multivalent bonding between flanking carboxylic groups and the magnetite surface, as suggested by FT-IR study. These findings are consistent with a report showing that PEG-oligo(aspartic acid) block copolymer-coated iron oxide nanoparticles were stable at pH 2–11 and in 1 M NaCl, where the repeating number of aspartic acid units was 3 or more [20]. In contrast, instability of Resovist® against salt addition may be due to weak interaction between magnetite and hydroxyl groups of dextran [21].

3.4. MR imaging of experimental pancreatic cancer in vivo

The MR imaging of tumor tissue *in vivo* was then conducted by comparing PEG–PAsp- and dextran-coated magnetite nanoparticles, Resovist®. Resovist® has already been approved for clinical use as a liver-specific MRI contrast agent, due to accumulation into the reticuloendothelial system (RES) of the normal liver. Most malignant liver tumors do not contain RES cells and therefore are contrasted positive by Resovist®. A xenografted BxPC3 human pancreatic adenocarcinoma cell line in nude mice, characterized histologically by fibrosis and hypovascularity, was used as a model of intractable cancer. Recently, we reported that the administration of TGF-β inhibitor to tumor model mice significantly enhanced the intratumoral accumulation of nanoparticles encapsulating anticancer drugs [11]. Thus, we tested the effect of the i.p. administration of TGF-β

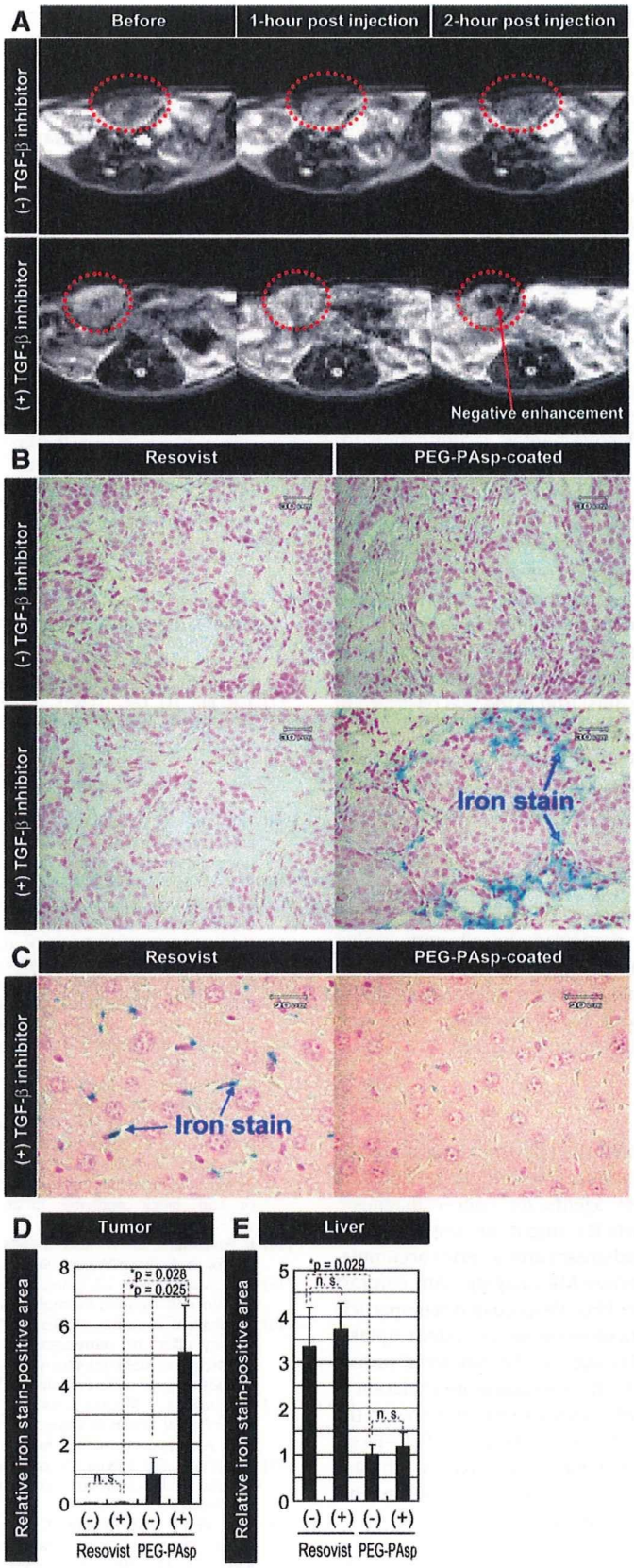

Fig. 6. MR imaging of experimental pancreatic cancer *in vivo* and the distribution of the nanoparticles in cancer and liver tissues. (A) T_2-weighted images of tumor-implanted mice (tumor sites are circled by red dotted line) at different temporal points after injection of PEG–PAsp-coated magnetite nanoparticles and TGF-β inhibitor. All images were obtained in a field strength of 4.7 T. (B) Histological sections of BxPC3 xenograft stained with Prussian blue. The distribution of Resovist® and PEG–PAsp-coated magnetite nanoparticles, at 5.5 mg/kg with and without TGF-β inhibitor at 1 mg/kg, were examined 24 h after the administration. (C) Histological sections of liver stained with Prussian blue. The distribution of Resovist® and PEG–PAsp-coated magnetite nanoparticles, at 5.5 mg/kg with TGF-β inhibitor at 1 mg/kg, was examined 24 h after the administration. (D and E) Areas of iron staining in the tumor and liver were quantified. PEG–PAsp, PEG–PAsp coated magnetite nanoparticles with (+) and without (−) inhibitor. Error bars in the graphs represent standard errors of the mean ($n = 6$), and P values were calculated by two-tailed Student's t test. n.s.: not significant.

inhibitor with the i.v. administration of Resovist® or the PEG–PAsp-coated magnetite nanoparticles on their imaging capability in size-matched xenografts of the BxPC3 cell line. Fig. 6A shows the T_2-weighted MR images of the tumors at different time periods after the intravenous administration (preinjection, and 1 and 2 h postinjection) of PEG–PAsp-coated magnetite nanoparticles with and without TGF-β inhibitor.

Resovist® failed to image the tumor even with the co-administration of TGF-β inhibitor, presumably due to the non-specific accumulation into the reticuloendothelial system [8]. In contrast, the PEG–PAsp-coated magnetite nanoparticles exhibited significant negative enhancement of signal intensity in the tumor region of T_2-weighted images when combined with TGF-β inhibitor, suggesting the accumulation of detectable amounts of the PEG–PAsp-coated magnetite nanoparticles within 2 h after injection. Therefore, the difference in behavior of these two types of magnetite nanoparticles *in vivo* had a crucial importance in achieving effective tumor accumulation for successful MR imaging.

To further verify the accumulation of iron oxide nanoparticles in the tumor, we performed Prussian blue staining of the tumor tissues to detect iron oxide, which stains blue. As shown in Fig. 6B, positive staining of the tumor for iron oxide was only obvious in the condition with PEG–PAsp-coated nanoparticles combined with the TGF-β inhibitor. Areas of iron staining in the tumor were then quantified as seen in Fig. 6D, demonstrating a significant increase in the areas of positive staining by TGF-β inhibitor treatment. The presence of iron oxide was consistent with the MRI results. Iron oxide was observed in the area rich in fibrotic components, suggesting that the administration of TGF-β inhibitor transiently increases the permeability of the tumor capillary to promote the extravasation of the PEG–PAsp-coated magnetite nanoparticles, even though the BxPC3 tumor has the characteristic of hypovascularity [11].

Lastly, we examined liver tissues from the mice treated with Resovist® or the PEG–PAsp-coated magnetite nanoparticle, with or without TGF-β inhibitor, by iron staining (Fig. 6C). Although aggregates of Resovist® accumulated in the liver, particularly in cells with smaller nuclei (presumably Kuppfer cells), far less PEG–PAsp-coated magnetite nanoparticles accumulated in the liver without aggregation. These results did not differ with or without TGF-β inhibitor, which was determined by the area of Prussian blue staining (Fig. 6E).

4. Conclusion

In conclusion, we here demonstrated the physicochemical properties of PEG–PAsp-coated magnetite nanoparticles and the feasibility of these nanoparticles as MR contrast agents for cancer diagnosis. Improving the stability of nanoparticles might be important for enabling a longer half-life in the bloodstream and a better accumulation in tumor tissue, leading to effective MR imaging with contrast agents. The neutral ζ-potential of the PEG–PAsp-coated nanoparticle may contribute to avoidance of reticuloendothelial system uptake. Formation of the stable and dense PEG layer on the magnetite surface through the anchoring of PEG–PAsp by the monodentate chelation of COO^- residues to iron atoms definitely plays a substantial role in the increased stability of the nanoparticles *in vivo*. The use of PEG–PAsp-coated magnetite nanoparticles combined with a TGF-β inhibitor could thus become a novel regime in the diagnosis of intractable cancers, including pancreatic adenocarcinoma.

Acknowledgements

The authors thank Dr James R. Christie II, The University of Tokyo, for editing the English of the manuscript. This work was supported by a Grant-in-Aid for Scientific Research from the Ministry of Education, Culture, Sports, Science and Technology (MEXT), Core Research for Evolution of Science and Technology (CREST), Japan Science and Technology Corporation (JST), and the 21st century COE program 'Human-Friendly Materials based on Chemistry' from MEXT.

Appendix A. Supplementary data

Supplementary data associated with this article can be found, in the online version, at doi:10.1016/j.jconrel.2009.06.002.

References

[1] M.R. Dreher, W. Liu, C.R. Michelich, M.W. Dewhirst, F. Yuan, A. Chilkoti, Tumor vascular permeability, accumulation, and penetration of macromolecular drug carriers, J. Natl. Cancer Inst. 98 (5) (2006) 335–344.
[2] H.A. Burris, M.J. Moore, J. Andersen, M.R. Green, M.L. Rothenberg, M.R. Modiano, M.C. Cripps, R.K. Portenoy, A.M. Storniolo, P. Tarassoff, R. Nelson, F.A. Dorr, C.D. Stephens, D.D. Von Hoff, Improvements in survival and clinical benefit with gemcitabine as first-line therapy for patients with advanced pancreas cancer: a randomized trial, J. Clin. Oncol. 15 (6) (1997) 2403–2413.
[3] D.V. Sahani, Z.K. Shah, O.A. Catalano, G.W. Boland, W.R. Brugge, Radiology of pancreatic adenocarcinoma: current status of imaging, J. Gastroenterol. Hepatol. 23 (1) (2008) 23–33.
[4] D.L. Huber, Synthesis, properties, and applications of iron nanoparticles, Small 1 (5) (2005) 482–501.
[5] R. Weissleder, G. Elidonzo, J. Wittenberg, C.A. Rabito, H.H. Bengele, L. Josephson, Ultrasmall superparamagnetic iron oxide: characterization of a new class of contrast agents for MR imaging, Radiology 175 (2) (1990) 489–493.
[6] M. Lewin, N. Carlesso, C.H. Tung, X.W. Tang, D. Cory, D.T. Scadden, R. Weissleder, Tat peptide-derivatized magnetic nanoparticles allow *in vivo* tracking and recovery of progenitor cells, Nat. Biotechnol. 18 (4) (2000) 410–414.
[7] Y.W. Jun, J.H. Lee, J. Cheon, Chemical design of nanoparticle probes for high-performance magnetic resonance imaging, Angew. Chem. Int. Ed. 47 (28) (2008) 5122–5135.
[8] D.D. Stark, R. Weissleder, G. Elizondo, et al., Superparamagnetic iron oxide: clinical application as a contrast agent for MR imaging of the liver, Radiology 168 (2) (1988) 297–301.
[9] T. Neuberger, B. Schöpf, H. Hofmann, M. Hofmann, B. von Rechenberg, Superparamagnetic nanoparticles for biomedical applications: possibilities and limitations of a new drug delivery system, J. Magn. Mater. 293 (1) (2005) 483–496.
[10] M. Kumagai, Y. Imai, T. Nakamura, Y. Yamasaki, M. Sekino, S. Ueno, K. Hanaoka, K. Kikuchi, T. Nagano, E. Kaneko, K. Shimokado, K. Kataoka, Iron hydroxide nanoparticles coated with poly(ethylene glycol)–poly(aspartic acid) block copolymer as novel magnetic resonance contrast agents for *in vivo* cancer imaging, Colloids Surf. B: Biointerfaces 56 (1–2) (2007) 174–181.
[11] M.R. Kano, Y. Bae, C. Iwata, Y. Morishita, M. Yashiro, M. Oka, T. Fujii, A. Komuro, K. Kiyono, M. Kaminishi, K. Hirakawa, Y. Ouchi, N. Nishiyama, K. Kataoka, K. Miyazono, Improvement of cancer-targeting therapy, using nanocarriers for intractable solid tumors by inhibition of TGF-β signaling, Proc. Natl. Acad. Sci. U. S. A. 104 (9) (2007) 3460–3465.
[12] Y. Matsumura, H. Maeda, A new concept for macromolecular therapeutics in cancer-chemotherapy-mechanism of tumoritropic accumulation of proteins and the antitumor agent SMANCS, Cancer Res. 46 (12) (1986) 6387–6392.
[13] N. Nishiyama, M. Yokoyama, T. Aoyagi, T. Okano, Y. Sakurai, K. Kataoka, Preparation and characterization of self-assembled polymer-metal complex micelle from cis-dichlorodiammineplatinum(II) and poly(ethylene glycol)–poly(alpha,beta-aspartic acid) block copolymer in an aqueous medium, Langmuir 15 (2) (1999) 377–383.
[14] E. Fukushima, S.B.W. Roeder (Eds.), Experimental pulse NMR: a nuts and bolts approach, Addison-Wesley, Reading, Mass, 1981, pp. 28–35.
[15] A.J.S. MacFadzean, L.J. Davis, Iron-staining erythrocytic inclusions with especial reference to acquired haemolytic anaemia, Glasgow Med. J. 28 (1947) 237–279.
[16] S. Takae, Y. Akiyama, H. Otsuka, T. Nakamura, Y. Nagasaki, K. Kataoka, Ligand density effect on biorecognition by PEGylated gold nanoparticles: regulated interaction of RCA120 lectin with lactose installed to the distal end of tethered PEG strands on gold surface, Biomacromolecules 6 (2) (2005) 818–824.
[17] L. Cromières, V. Moulin, B. Fourest, E. Giffaut, Physico-chemical characterization of the colloidal hematite/water interface: experimentation and modeling, Colloids Surf., A. Physicochem. Eng. Asp. 202 (1) (2002) 101–115.
[18] L.J. Kirwan, P.D. Fawell, W. van Bronswijk, In situ FTIR-ATR examination of poly (acrylic acid) adsorbed onto hematite at low pH, Langmuir 19 (14) (2003) 5802–5807.
[19] Y.X.J. Wang, S.M. Hussain, G.P. Krestin, Superparamagnetic iron oxide contrast agents: physicochemical characteristics and applications in MR imaging, Eur. Radiol. 11 (11) (2001) 2319–2331.
[20] S.R. Wan, J.S. Huang, M. Guo, H. Zhang, Y. Cao, H. Yan, K. Liuet, Biocompatible superparamagnetic iron oxide nanoparticle dispersions stabilized with poly (ethylene glycol)oligo(aspartic acid) hybrids, J. Biomed. Mater. Res. A 80A (4) (2007) 946–954.
[21] C.W. Jung, Surface-properties of superparamagnetic iron-oxide MR contrast agents — ferumoxides, ferumoxtran, ferumoxsil, Magn. Reson. Imaging 13 (5) (1995) 675–691.

Enhanced Percolation and Gene Expression in Tumor Hypoxia by PEGylated Polyplex Micelles

Muri Han[1], Makoto Oba[2], Nobuhiro Nishiyama[3,4], Mitsunobu R Kano[4,5], Shinae Kizaka-Kondoh[6] and Kazunori Kataoka[1,3,4,7]

[1]Department of Materials Engineering, Graduate School of Engineering, The University of Tokyo, Tokyo, Japan; [2]Department of Clinical Vascular Regeneration, Graduate School of Medicine, The University of Tokyo, Tokyo, Japan; [3]Center for Disease Biology and Integrative Medicine, Graduate School of Medicine, The University of Tokyo, Tokyo, Japan; [4]Center for NanoBio Integration, The University of Tokyo, Tokyo, Japan; [5]Department of Molecular Pathology, Graduate School of Medicine, The University of Tokyo, Tokyo, Japan; [6]Department of Radiation Oncology and Image-Applied Therapy, Kyoto University, Graduate School of Medicine, Kyoto, Japan; [7]Core Research for Evolutional Science and Technology (CREST), Japan Science and Technology Agency (JST), Kawaguchi, Japan

In regard to gene vectors for cancer gene therapy, their percolation into the tumor tissue should be essential for successful outcome. Here, we studied the tumor penetrability of nonviral vectors (polyplexes) after incubation with the multicellular tumor spheroid (MCTS) models and intratumoral (i.t.) injection into subcutaneous tumors. As a result, polyethylene glycolated (PEGylated), core–shell type polyplexes (polyplex micelles) showed facilitated percolation and improved transfection inside the tumor tissue, whereas conventional polyplexes from cationic polymers exhibited limited percolation and localized transfection. Furthermore, the transfection of hypoxia-responsive plasmid demonstrated that polyplex micelles allowed the transfection to the hypoxic region of the tumor tissue in both *in vitro* and *in vivo* experiments. To the best of our knowledge, our results demonstrated for the first time that polyplex micelles might show improved tumor penetrability over cationic polyplexes, thereby achieving transfection into the inside of the tumor tissue.

Received 22 December 2008; accepted 24 April 2009; published online 26 May 2009. doi:10.1038/mt.2009.119

INTRODUCTION

Gene therapy is a promising method for the treatment of malignant tumors, and its success relies on the capabilities of gene vectors. In this regard, nonviral vectors composed of plasmid DNA (pDNA) and cationic polymers, so-called polyplexes have been attracting much attention due to several advantages such as no immunogenicity, safety, and easy large-scale preparation.[1–4] So far, considerable efforts have been devoted to improve the transfection efficiency of polyplexes as well as control the gene expression in the body.[5–8] However, in regard to gene vectors for cancer gene therapy, much attention should be paid on another important property: percolation into the tumor tissue. In general, solid tumors are known to possess heterogeneous structures composed of blood vessels, interstitial tissues, clusters of tumor cells with normoxic and hypoxic regions. Therefore, it might be difficult to deliver the therapeutic agents to tumor cells distant from the vasculature.[9–11] Furthermore, hypoxic region induced by the insufficient blood supply is known to be inherently less susceptible to therapeutic agents.[10] As such difficulty in treating hypoxic regions is often correlated with recurrence and malignant progression of solid tumors,[10] overcoming the limited drug access to hypoxic cells should be a critical issue in cancer therapy. Thus, the percolation of gene vectors in solid tumors should be of primary importance to achieve successful cancer gene therapy.

Recently, we have developed a highly transfectable but less-toxic core–shell type polyplex with poly(ethylene glycol) (PEG) palisades (polyplex micelle), which was formed through the electrostatic interaction between pDNA and PEG-*b*-polyaspartamide having 1,2-diaminoethane side chain (PEG-*b*-P[Asp(DET)]) (**Figure 1**).[12,13] This polyplex micelle showed remarkable features, including efficient gene transfer to primary cells,[12] successful *in vivo* transfection to a rabbit carotid artery,[14] and transfection-mediated bone regeneration.[15] In this study, we explored the tumor penetrability of polyplex micelles, because we have recently demonstrated that amphiphilic block copolymer micelles can show penetrability into multicellular tumor spheroids (MCTSs)[16] as well as solid tumors after intravenous administration.[17] Here, we demonstrated that polyplex micelles from PEG-*b*-P[Asp(DET)] showed successful transfection to hypoxic cells inside MCTS as well as enhanced percolation and widely distributed gene expression within the tumor tissue after intratumoral (i.t.) injection. In contrast, cationic polyplexes showed limited penetration and localized transfection in both *in vitro* and *in vivo* studies. These results suggest that polyplex micelles may overcome the transport barrier of nonviral vectors, facilitating their use for cancer gene therapy.

RESULTS

Transfection to MCTS

MCTS is an appropriate *in vitro* tumor model representing morphological and functional features of *in vivo* avascular solid tumors, and is composed of actively proliferating outer cell layers

Correspondence: *Kazunori Kataoka, Department of Materials Engineering, Graduate School of Engineering, The University of Tokyo, 7-3-1 Hongo, Bunkyo-ku, Tokyo 113-8656, Japan. E-mail: kataoka@bmw.t.u-tokyo.ac.jp*

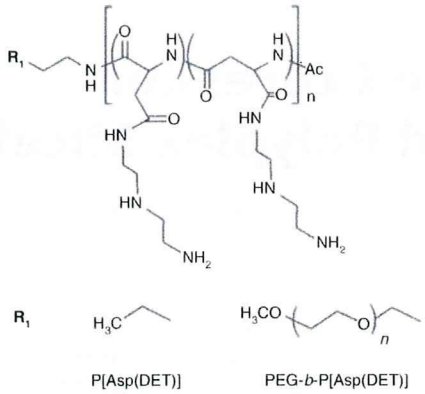

Figure 1 Chemical structures of P[Asp(DET)] homopolymers and PEG-*b*-P[Asp(DET)] block copolymers.

and hypoxic and quiescent inner cells.[18] In this study, a large-sized MCTS (400–500 μm), which possessed a hypoxic region characterized by necrotic cells inside due to limited supply of oxygen and nutrition (**Figure 2a**), was transfected with pCAcc + *Venus* by using the linear polyethylenimine (LPEI) and P[Asp(DET)] polyplexes and PEG-*b*-P[Asp(DET)] polyplex micelles at a defined mixing ratio of the number of amino groups units to a nucleotide unit (N/P ratio). Note that, although we have recently reported that a small-sized MCTS (~100 μm) can be disrupted by the cytotoxicity of polyplexes,[19] the large-sized MCTS used in this study is stable against the polyplex-mediated transfection. The expression of a variant of yellow fluorescent protein, *Venus* was evaluated by confocal microscopic observation. At 48 hours after the transfection (24-hour incubation and additional 24-hour incubation after the medium replacement), the LPEI polyplexes (N/P = 6, the manufacturer's recommendation ratio) and P[Asp(DET)] polyplexes (N/P = 20) showed significant gene expression limited to the periphery of the MCTS (**Figure 2b**). This result indicates that cationic polyplexes might lack the ability to transfect the inside of the MCTS. In contrast, PEG-*b*-P[Asp(DET)] polyplex micelles (N/P = 20) showed appreciable gene expression at not only the periphery but also the inside of the MCTS (**Figure 2b**), where a great number of necrotic cells were observed as indicated by red fluorescence from ethidium homodimer (EthD-1) (**Figure 2c**). These results suggest that polyplex micelles may allow the gene transfer to tumor cells in the hypoxic inner region of the MCTS.

Hypoxia-selective gene expression in the MCTS

To confirm the gene expression in hypoxic cells in the MCTS, we carried out the transfection study using pDNA encoding *Venus* driven by the 5× hypoxia-responsive element (5HRE) promoter (p5HRE + *Venus*). The hypoxia-selectivity of p5HRE + *Venus* was examined in monolayer cultured HuH-7 cells under hypoxic conditions reproduced by iron-chelating agent, deferoxamine mesylate.[20] As shown in **Figure 3a**, PEG-*b*-P[Asp(DET)] polyplex micelles containing hypoxia-responsive p5HRE + *Venus* showed no gene expression under normoxic conditions (0 μmol/l deferoxamine mesylate) but an appreciable gene expression under hypoxia-mimicking conditions (200 μmol/l deferoxamine mesylate). Note that polyplex micelles containing hypoxia-irresponsive pCAcc + *Venus* exhibited significant

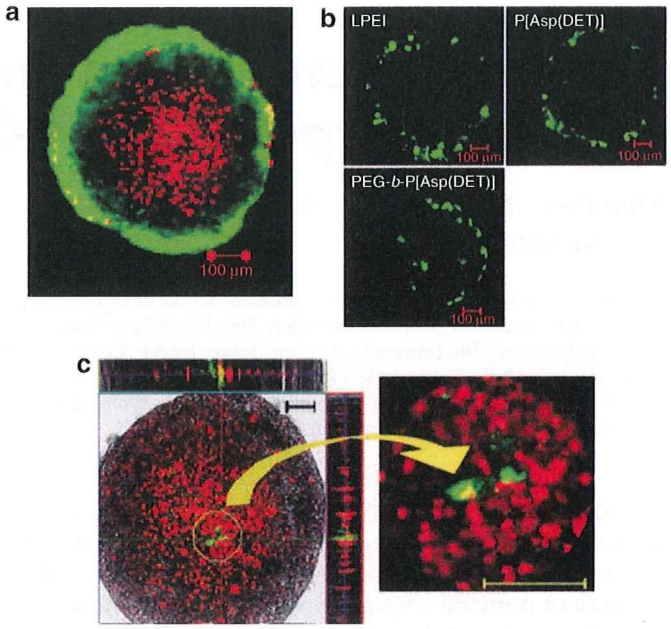

Figure 2 Transfection to HuH-7 MCTS. (**a**) Live/dead staining of HuH-7 spheroid (optical slice at the middle of spheroid. Bar = 100 μm). The green and red fluorescence are derived from live and dead cells, respectively. (**b**) Gene expression of pCAcc + *Venus* in HuH-7 MCTS transfected with LPEI polyplexes (N/P = 6), P[Asp(DET)] polyplexes (N/P = 20), and PEG-*b*-P[Asp(DET)] polyplex micelles (N/P = 20) (24 hours of incubation time and 24 hours of additional incubation after the medium replacement). (**c**) Gene expression of pCAcc + *Venus* at the inner region of HuH-7 MCTS transfected with PEG-*b*-P[Asp(DET)] polyplex micelles (N/P = 20) (24 hours of incubation time and 24 hours of additional incubation after the medium replacement) (Left: The red and green fluorescence are derived from dead cells and transfected protein *Venus*, respectively. Right: Magnified image of the circled region in the left picture). LPEI, linear polyethylenimine; MCTS, multicellular tumor spheroid; N/P, ratio of the number of amino groups units to a nucleotide unit.

gene expression under both normoxic and hypoxic conditions. Thus, p5HRE + *Venus* was demonstrated to be highly selective to hypoxic environments. Then, LPEI and P[Asp(DET)] polyplexes and PEG-*b*-P[Asp(DET)] polyplex micelles containing p5HRE + *Venus* were applied to the transfection to the large-sized MCTS (400–500 μm). As a result, none of 5 spheroids transfected with LPEI polyplexes showed the expression of p5HRE + *Venus* (data not shown), which may be consistent with the expression of pCAcc + *Venus* limited to the periphery of the MCTS (**Figure 2b**). Surprisingly, P[Asp(DET)] polyplexes exhibited the expression of p5HRE + *Venus* in two of five spheroids at 48 hours after the transfection; however, the gene expression was limited to the outer rims of hypoxic regions at ~100 μm distance from the periphery of the MCTS (**Figure 3b**; the yellow circle is the initial size of spheroids before the transfection). This result suggests that P[Asp(DET)] polyplexes could penetrate into the inside of the spheroids to some extent. In contrast, PEG-*b*-P[Asp(DET)] polyplex micelles allowed the transfection of p5HRE + *Venus* to a larger number of the cells in the inner region of the MCTS in 7 of 10 spheroids (**Figure 3b**), suggesting the ability of the polyplex micelles to transfect hypoxic cells inside of the spheroids. To further confirm this effect, two distinct plasmids encoding DsRedC1 (red fluorescence) driven

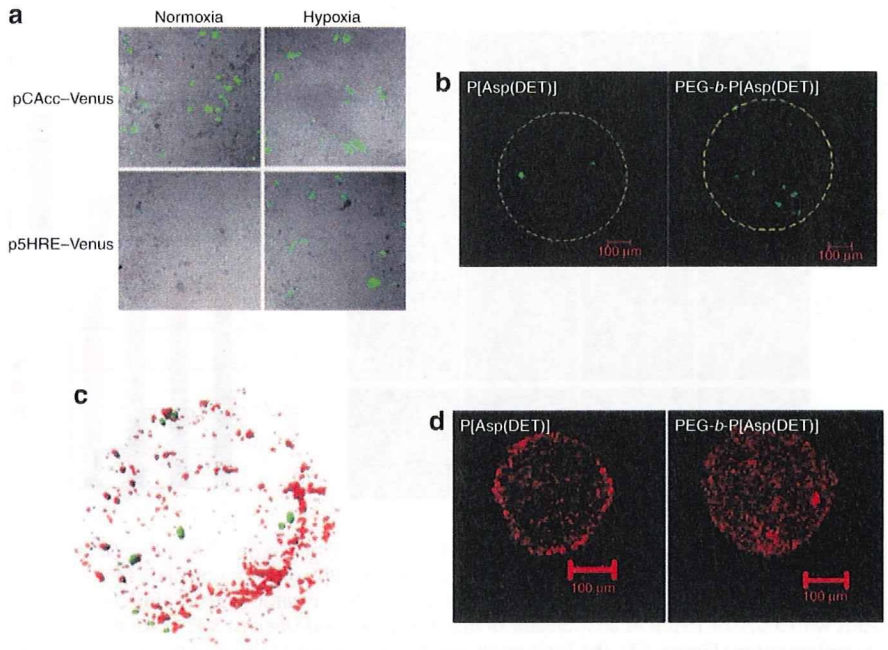

Figure 3 Hypoxia selective gene expression in the MCTS. (**a**) Gene expressions of hypoxia-irresponsive pCAcc + *Venus* and hypoxia-responsive p5HRE + *Venus* in monolayer cultured HuH-7 cells under normoxic and hypoxic conditions. HuH-7 cells were incubated with PEG-*b*-P[Asp(DET)] polyplex micelles (N/P = 20) for 24 hours, followed by additional 24 hours incubation after the medium replacement. Hypoxia-mimicking conditions were reproduced by incubating the cells with iron chelating agent, DFx during the postincubation. (**b**) Gene expressions of hypoxia-responsive p5HRE + *Venus* in the HuH-7 spheroids transfected with P[Asp(DET)] polyplexes and PEG-*b*-P[Asp(DET)] polyplex micelles (N/P = 20). The yellow circle indicates the size of the MCTS at the time of the transfection. (**c**) Piled up images of the gene expressions of hypoxia-irresponsive pCMV-DsRedC1 (red fluorescence) and hypoxia-responsive p5HRE – *Venus* (green fluorescence) in the MCTS transfected with PEG-*b*-P[Asp(DET)] polyplex micelles incorporating each plasmid (N/P = 20). (**d**) Distribution of Cy3-labeled pDNA encapsulated into P[Asp(DET)] polyplexes (N/P = 20) and PEG-*b*-P[Asp(DET)] polyplex micelles (N/P = 20) in HuH-7 MCTS after 24-hour incubation. The images were taken at the center of the spheroids. DFx, deferoxamine mesylate; MCTS, multicellular tumor spheroid; N/P, ratio of the number of amino groups units to a nucleotide unit.

by the cytomegalovirus (CMV) promoter (pCMV-DsRedC1) and *Venus* (green fluorescence) driven by the 5HRE promoter (p5HRE – *Venus*) were independently encapsulated into PEG-*b*-P[Asp(DET)] polyplex micelles, and then applied to the transfection to the MCTS. After 48 hours, optical slices of the MCTS at a depth of 1 μm were taken by confocal microscopy, and then piled up by Imaris software (Carl Zeiss, Jena, Germany) to obtain the three-dimensional localization of each fluorescence. As shown in **Figure 3c**, the expression of p5HRE – *Venus* was mainly detected in the inner region of the MCTS, whereas the expression of pCMV-DsRedC1 was observed throughout the MCTS. Thus, the hypoxic inner regions of the MCTS were successfully transfected with PEG-*b*-P[Asp(DET)] polyplex micelles.

Percolation of polyplexes and polyplex micelles into the MCTS

The percolation of the polyplexes and polyplex micelles into the MCTS was investigated by using Cy3-labeled pDNA. In this study, the MCTS with a diameter of 200–250 μm was used to detect weak fluorescence from Cy3-labeled pDNA within the spheroids. **Figure 3d** shows the fluorescent image of Cy3-labeled pDNA at the center of HuH-7 MCTS after 24-hour incubation with polyplexes or polyplex micelles. Note that the treatment of the relatively small-sized MCTS with LPEI polyplexes resulted in destruction of spheroid structures due to the cytotoxicity of LPEI as previously reported.[19] As shown in **Figure 3d**, P[Asp(DET)] polyplexes displayed apparent fluorescence at the periphery of spheroids. This result is consistent with the previous report that cationic polyplexes could penetrate only the outer 3–5 proliferating cell layers (10–20 μm) of the MCTS.[11] In contrast, the pDNA formulated in PEG-*b*-P[Asp(DET)] polyplex micelles showed well-distributed fluorescence within spheroids, suggesting their percolation into the inside of the spheroids. Similar results were obtained when the MCTS model from a different cell line (*i.e.*, human pancreatic BxPC3 cells) were used (**Supplementary Figure S1**). Thus, polyplex micelles might possess the ability to percolate into the spheroids over cationic polyplexes.

i.t. distribution of polyplexes and polyplex micelles after i.t. injection

The i.t. distribution of naked pDNA, LPEI polyplexes (N/P = 6), P[Asp(DET)] polyplexes (N/P = 20), or PEG-*b*-P[Asp(DET)] polyplex micelles (N/P = 20) after the injection to solid tumors (human pancreatic adenocarcinoma BxPC3 cells) was evaluated by using Cy3-labeled pDNA (n = 3). In this experiment, each formulation was coadministered with FluoSphere fluorescent microspheres [particle size: 15 μm, 645 nm/680 nm (Ex/Em)] as a marker for the injection point. The fluorescent images of Cy3-labeled pDNA in BxPC3 tumors are shown in **Figure 4a** and **Supplementary Figure S2**, and the total pixels of fluorescence area and its localization in the three different regions classified by the distance from the injection point (<100 μm, 100–200 μm, >200 μm) are quantified

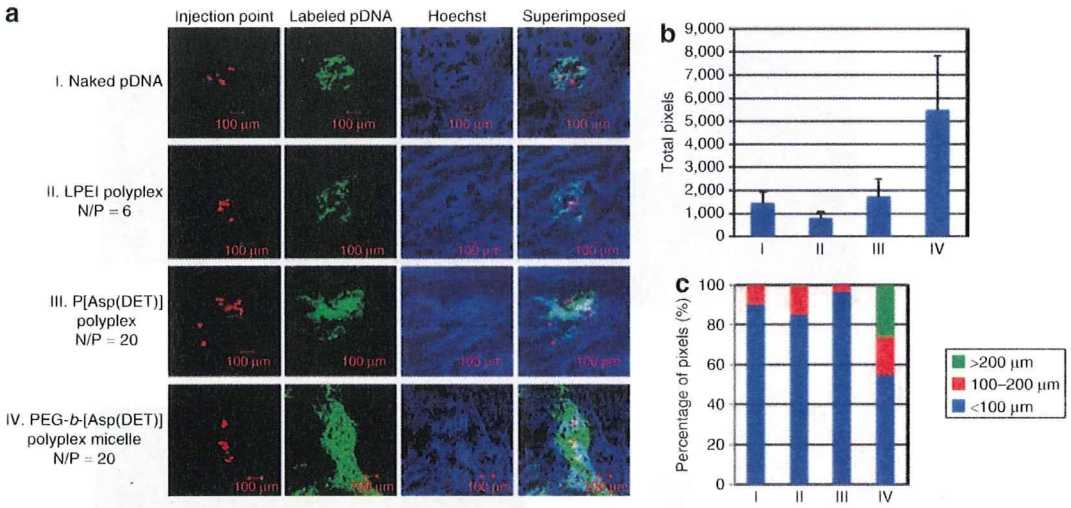

Figure 4 Intratumoral distribution of polyplexes and polyplex micelles after intratumoral injection. (**a**) Distribution of Cy3-labeled pDNA (green fluorescence) in a naked form or encapsulated into LPEI polyplexes (N/P = 6), P[Asp(DET)] polyplexes (N/P = 20), or PEG-*b*-P[Asp(DET)] polyplex micelles (N/P = 20) within human pancreatic adenocarcinoma BxPC3 tumors after intratumoral (i.t.) injection. The red and blue fluorescence are derived from fluorescent beads with a size of 15 μm as an indicator of injection point and Hoechst 33342 for the nuclear staining, respectively (more detailed data are shown in **Supplementary Figure S2**). (**b**) Total pixels and (**c**) percentage of pixels of fluorescent area of Cy3-labeled pDNA in three regions classified by the distance from the injection point. N/P, ratio of the number of amino groups units to a nucleotide unit.

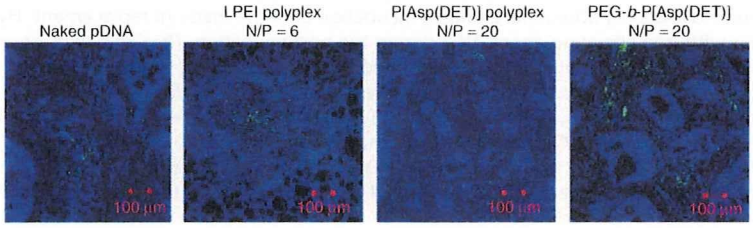

Figure 5 Gene expression of EGFP (green) within BxPC3 tumors at 6 days post-i.t. injection of naked plasmids, LPEI polyplexes (N/P = 6), P[Asp(DET)] polyplexes (N/P = 20), or PEG-b-P[Asp(DET)] polyplex micelles (N/P = 20). The blue fluorescence is derived from Hoechst 33342 for the nuclear staining. EGFP, enhanced green fluorescent protein; LPEI, linear polyethylenimine; N/P, ratio of the number of amino groups units to a nucleotide unit.

in Figure 4b,c, respectively. As a result, PEG-*b*-P[Asp(DET)] polyplex micelles showed a tendency to distribute more widely from the injection point compared with naked pDNA, LPEI and P[Asp(DET)] polyplexes. Note that irregular i.t. distribution of the polyplex micelles may be attributed to the heterogeneous structure of the BxPC3 tumors comprising clusters of dense tumor cells and interstitial tissues as indicated by the nuclear staining with Hoechst 33342.

In vivo gene expression after i.t. injection

The *in vivo* gene expression of fluorescent protein, enhanced green fluorescent protein (EGFP) within the BxPC3 tumors at 6 days post-i.t. injection of naked pDNA, LPEI polyplexes (N/P = 6), P[Asp(DET)] polyplexes (N/P = 20), or PEG-*b*-P[Asp(DET)] polyplex micelles (N/P = 20) was evaluated (n = 3). Note that P[Asp(DET)] polyplexes and polyplex micelles showed the highest transfection at 6 days postincubation in the MCTS models.[19] As shown in Figure 5, PEG-*b*-P[Asp(DET)] polyplex micelles apparently showed a widely distributed expression of EGFP in comparison with naked pDNA, LPEI, and P[Asp(DET)] polyplexes. These results seem to be consistent with the i.t. distribution of polyplex micelles (Figure 4).

Furthermore, the expression of hypoxia-responsive p5HRE + *Venus* within the BxPC3 tumors was evaluated (Figure 6a). The hypoxic region developed far from the vessels in the BxPC3 tumors was confirmed by fluorescein isothiocyanate-conjugated anti-Hypoxyprobe-1 monoclonal antibody (Figure 6b). Similar to Figure 4c, the pixels of fluorescent area in Figure 6a are classified into three different regions and summarized in Figure 6c. As a result, naked pDNA and LPEI polyplexes showed little gene expression, and P[Asp(DET)] polyplexes showed an appreciable gene expression in the region close to the injected point. In contrast, PEG-*b*-P[Asp(DET)] polyplex micelles showed well-distributed gene expression even in the furthest region from the injection point (>200 μm). These results suggest that the polyplex micelles might have the ability to percolate into the tumor tissue, thereby improving the gene transfection in the hypoxic regions of solid tumors.

DISCUSSION

Recently, we compared the transfection ability and cytotoxicity between P[Asp(DET)] polyplexes and PEG-*b*-P[Asp(DET)] polyplex micelles by using MCTS models.[19] We revealed that the PEGylation decreased the cytotoxicity of polyplexes without

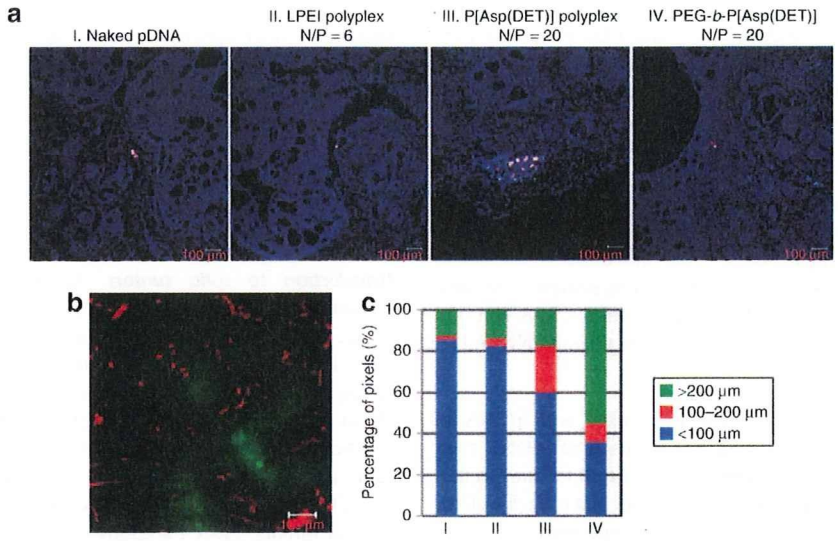

Figure 6 Hypoxia-responsive gene expression after intratumoral injection. (**a**) Gene expression of hypoxia-responsive p5HRE + *Venus* (white) within BxPC3 tumors at 6 days post-i.t. injection of naked plasmids, LPEI polyplexes (N/P = 6), P[Asp(DET)] polyplexes (N/P = 20), or PEG-b-P[Asp(DET)] polyplex micelles (N/P = 20). The red and blue fluorescence are derived from fluorescent beads with a size of 15 μm as an indicator of injection point and Hoechst 33342 for the nuclear staining, respectively. (**b**) Hypoxic regions in BxPC3 solid tumors. The red and green fluorescence are derived from anti-PECAM-1 antibody and anti-Hypoxyprobe-1 antibody, respectively. (**c**) Percentage of pixels of fluorescent area of transfected *Venus* protein in three regions classified by the distance from the injection point. i.t., intratumoral; LPEI, linear polyethylenimine; N/P, ratio of the number of amino groups units to a nucleotide unit.

compromising the transfection efficiency, while delaying the onset of gene expression. In this study, we report another important property of PEG-*b*-P[Asp(DET)] polyplex micelles, *i.e.*, tissue penetrability. We demonstrated that polyplex micelles showed facilitated percolation of loaded pDNA into the tumor tissue in both *in vitro* MCTS models and subcutaneous tumor models. Consequently, polyplex micelles showed a well-distributed gene expression after i.t. injection, allowing the transfection to the hypoxic regions of the tumors. These observations are in good agreement with our previous reports that polymeric micelles incorporating adriamycin showed enhanced percolation into the tumor tissue not only in the MCTS models[16] but also in subcutaneous tumors after intravenous administration.[17] Recently, Mellor *et al.* reported that cationic polyplexes from linear and branched PEI and lipoplexes showed penetration and transfection limited to the outer 3–5 proliferating cell layers in the large-sized MCTS (~474 nm).[11] Consistently, our results (**Figures 2b, 3d**, and **4–6**) also demonstrated not only *in vitro* but also *in vivo* that cationic polyplexes might show the limited penetration and localized transfection within the tumor. Furthermore, the result indicates for the first time that PEGylated polyplexes led loaded pDNA to show improved tissue penetrability compared with cationic polyplexes, exerting the appreciable gene expression in the inner hypoxia region.

PEGylation has apparently an advantage to prevent aggregation of polyplexes in the physiological condition with the presence of considerable amount of salt. Also, the PEGylation effectively masks the cationic nature of the core polyplexes, preventing nonspecific interaction serum proteins and extracellular matrices. Indeed, we observed that the PEG shielding of the P[Asp(DET)] polyplexes decreased the Zeta-potential from +30 mV to +6 mV. Such prevention of aggregate formation and reduced interaction with biological components by PEGylation may contribute to the facilitated percolation of the polyplexes into the tumor tissue. In this regard, the stability of polyplex micelles is an important issue during their penetration process into the tumor tissue. Our previous study revealed that the PEG-*b*-P[Asp(DET)] polyplex micelles showed much higher tolerability against the pDNA exchange reaction with an anionic lipid compared with the P[Asp(DET)] polyplexes.[19] Such increased stability of polyplex micelles is consistent with their improved penetration into the tumor tissue observed here. Furthermore, there are several reports that PEGylated nanoparticles show enhanced passage through the mucosal tissues to overcome intestinal barriers presumably due to the high flexibility and amphiphilicity of PEG chains.[21–23]

The detailed mechanisms of the enhanced percolation of polyplex micelles in the tumor tissue remain to be clarified yet; however, the results in this study clearly demonstrate that polyplex micelles might access the tumor cells in the hypoxic region with the intrinsic functions to deliver therapeutic genes. Thus, polyplex micelles are expected to treat hypoxic regions in the tumor tissue, potentially preventing the recurrence and malignant progression of solid tumors. Together with improved pharmacokinetic parameters, PEGylated polyplexes with a high tissue-percolation property might be promising nonviral vectors for *in vivo* cancer gene therapy.

MATERIALS AND METHODS

Plasmid DNA. The plasmid, pCAcc vector having CAG promoter,[24] was provided by RIKEN Bioresource Center (Ibaraki, Japan). Also, a fragment cDNA of SEYFP-F46L (*Venus*), which is a variant of yellow fluorescent protein with the mutation F46L,[25] was provided by A. Miyawaki at the Brain Science Institute, RIKEN and inserted into the pCAcc vector (pCAcc + *Venus*). Each pDNA was amplified in competent DH5α *Escherichia coli* and purified using HiSpeed Plasmid MaxiKit (Qiagen Sciences, Hilden, Germany). The plasmid, pGL5 vector having p5HRE, was provided by Faculty of Medicine, Kyoto University (Japan).[26] The DNA fragment encoding *Venus* was inserted between *Hind*III and *Xba*I sites of pGL3/5xHRE/CMVmp.

Nonviral vectors. LPEI (ExGen 500, 22 kd) was purchased from Fermentas (Burlington, Ontario, Canada). P[Asp(DET)] and PEG-*b*-P[Asp(DET)] were prepared as previously reported.[12–14] Briefly, β-benzyl-L-aspartate *N*-carboxyanhydride was polymerized by the initiation from the primary amino group of *n*-butylamine and MeO-PEG-NH_2 (M_w: 12,000) to obtain poly(β-benzyl L-aspartate) (PBLA) and PEG-*b*-PBLA, respectively. The degree of polymerization of PBLA was determined to be 98 for PBLA and 101 for PEG-*b*-PBLA by the ^1H NMR measurement. Then, PBLA and PEG-*b*-PBLA were reacted with diethylenetriamine (DET) (50 equiv to benzyl group of PBLA segment) under mild anhydrous conditions to obtain P[Asp(DET)] and PEG-*b*-P[Asp(DET)], respectively. The unimodal distribution and the almost 100% conversion of the BLA unit into Asp(DET) unit were confirmed by gel permeation chromatography and ^1H NMR measurements.

Preparation of polyplexes. Each polymer was mixed with pDNA in 10 mmol/l Tris–HCl (pH 7.4) at varying N/P ratios (final pDNA concentration: 100 μg/ml). Polyplex was applied to each well for transfection 30 minutes after preparation. Polyplex micelle was applied to each well for transfection after overnight incubation at ambient temperature.

Cell culture and preparation of MCTS. Human hepatoma HuH-7 cells (from JCRB Cell Bank, Osaka, Japan) and human pancreatic adenocarcinoma BxPC3 cells (from ATCC, Manassas, VA) were maintained in Dulbecco's modified Eagle's medium and RPMI 1640 medium, respectively, supplemented with 10% fetal bovine serum in a humidified atmosphere containing 5% CO_2 at 37 °C. MCTS were prepared by using the plate designed for spheroid formation (Sumiloncelltight; Sumitomo Bakelite, Tokyo, Japan) as reported previously.[15,18] The size of MCTS can be controlled by the incubation period. During the incubation, the medium was replaced by fresh medium containing 10% fetal bovine serum every 3 days.

Live/dead assay. Live and dead assay was accomplished with the Live/Dead kit protocol (Molecular Probes, Carlsbad, CA). MCTS was rinsed with PBS(−) and then incubated with a solution containing 0.8 μmol/l calcein AM [495 nm/515 nm (Ex/Em)] and 4 μmol/l EthD-1 (495 nm/635 nm) in PBS(−) for 3 hours at 37 °C, followed by the observation by LSM 510 confocal laser scanning microscope (CLSM) (Carl Zeiss).

Transfection to MCTS. MCTS was incubated for 6–8 days until the diameter became >400–500 μm. Then, each polyplex solution containing 1 μg pDNA was applied to each well for the transfection. After 24-hour incubation, the medium was replaced by fresh medium, followed by additional 24-hour incubation. The gene expression of the *Venus* or EGFP was then evaluated through the observation by CLSM.

Percolation of nonviral vectors into the MCTS. To visualize the distribution of nonviral vectors in MCTS, pDNA was labeled with Label IT Cy3 Labeling Kit (Mirus, Piscataway, NJ). In this experiment, MCTS with the diameter of 200–250 μm was incubated with polyplexes or polyplex micelles containing 1 μg Cy3-labeled pDNA for 24 hours. After 24-hour incubation, MCTS was harvested and rinsed, followed by observation by CLSM.

Animal models. BALB/c nude mice (female, 5 weeks old) were obtained from Charles River Laboratories (Tokyo, Japan). BxPC3 cells (5×10^6 cells in 100 μl of PBS) were injected subcutaneously into the BALB/c nude mice and allowed to grow for 2–3 weeks to reach the proliferative phase. All animal experimental protocols were performed in accordance with the policies of the Animal Ethics Committee of the University of Tokyo.

Percolation of nonviral vectors in solid tumors. After the tumor size reached 6–8 mm in a diameter, the mice received the i.t. injection of 2 μg Cy3-labeled pDNA in a naked or polyplex-encapsulated form [20 μl in 10 mmol/l HEPES buffer (pH 7.4)] by using the Hamilton Microliter Syringe (Hamilton, Reno, NV). In this experiment, 5 μl of FluoSpheres fluorescent microspheres (particle size: 15 μm, 645 nm/680 nm) were mixed with Cy3-labeled pDNA solution and simultaneously injected into the BxPC3 tumor for indication of the injection point. After 24 hours, the tumors were excised and fixed with 10% formalin and sucrose PBS(−), followed by freezing in dry-iced acetone. Frozen samples were sectioned at 10-μm thickness in a cryostat, and stained with Hoechst 33342 (Dojindo Laboratories, Tokyo, Japan). The fluorescent images were then observed by CLSM.

Transfection to solid tumors. According to the protocols for the percolation study, the tumor-bearing mice received the i.t. injection of 2 μg pCAcc + EGFP or p5HRE + *Venus* in a naked or polyplex-encapsulated form. The animals administered with pCAcc + EGFP were killed at 6 days postinjection, and the excised tumors were fixed as previously described. The fluorescence of frozen section of solid tumors was observed by CLSM. On the other hand, the animals administered with p5HRE + *Venus* were administered with Hypoxyprobe-1 (Millipore Chemicon, Billerica, MA) at 60 mg/kg via tail vein at 6 days postinjection, and then killed for removal of solid tumors. Frozen sections of the xenograft were stained with rat anti-PECAM-1 antibody (BD Pharmingen, Franklin Lakes, NJ), and subsequently stained with Alexa 594-conjugated anti-rat IgG antibody (Invitrogen Molecular Probes, Carlsbad, CA) and fluorescein isothiocyanate-conjugated anti-Hypoxyprobe-1 MAb. The section was further counter-stained with TOTO-3 (Invitrogen Molecular Probes), and the fluorescence images were captured by CLSM.

Quantitative analysis of fluorescent images. The pixels of fluorescent area of Cy3-labeled pDNA or transfected *Venus* protein in the tumor section were quantified by using the Image J software (http://rsb.info.nih.gov/ij/), and classified into three different regions by the distance from the injection point (<100 μm, 100–200 μm, >200 μm).

SUPPLEMENTARY MATERIAL

Figure S1. Distribution of labeled pDNA in BxPC3 MCTS transfected by each polyplex or polyplex micelles in intersectional profiles at the shown slices (Optical slice at the center of MCTS. Red fluorescence is Cy3 labeled-pDNA).

Figure S2. Distribution of Cy3-labeled pDNA (green fluorescence) in a naked form or encapsulated into LPEI polyplexes (N/P=6), P[Asp(DET)] polyplexes (N/P=20) or PEG-*b*-P[Asp(DET)] polyplex micelles (N/P=20) within human pancreatic adenocarcinoma BxPC3 tumors after the intratumoral injection.

ACKNOWLEDGMENTS

We thank Kotoe Date (the University of Tokyo) for technical assistance. This work was supported in part by the Core Research Program for Evolutional Science and Technology from Japan Science and Technology Agency.

REFERENCES

1. Boussif, O, Lezoualc'h, F, Zanta, MA, Mergny, MD, Scherman, D, Demeneix, B *et al.* (1995). A versatile vector for gene and oligonucleotide transfer into cells in culture and *in vivo*: polyethylenimine. *Proc Natl Acad Sci USA* **92**: 7297–7301.
2. Ogris, M and Wagner, E (2002). Targeting tumors with non-viral gene delivery systems. *Drug Discov Today* **7**: 479–485.
3. Merdan, T, Kopecek, J and Kissel, T (2002). Prospects for cationic polymers in gene and oligonucleotide therapy against cancer. *Adv Drug Deliv Rev* **54**: 715–758.
4. Pack, DW, Hoffman, AS, Pun, S and Stayton, PS (2005). Design and development of polymers for gene delivery. *Nat Rev Drug Discov* **4**: 581–593.
5. Erbacher, P, Roche, AC, Monsigny, M and Midoux, P (1995). Glycosylated polylysine/DNA complexes: gene transfer efficiency in relation with the size and the sugar substitution level of glycosylated polylysines and with the plasmid size. *Bioconjug Chem* **6**: 401–410.
6. Merdan, T, Callahan, J, Petersen, H, Kunath, K, Bakowsky, U, Kopecková, P *et al.* (2003). Pegylated polyethylenimine-Fab' antibody fragment conjugates for targeted gene delivery to human ovarian carcinoma cells. *Bioconjug Chem* **14**: 989–996.
7. Ogris, M, Brunner, S, Schüller, S, Kircheis, R and Wagner, E (1999). PEGylated DNA/transferrin-PEI complexes: reduced interaction with blood components, extended circulation in blood and potential for systemic gene delivery. *Gene Ther* **6**: 595–605.

8. Harada-Shiba, M, Yamauchi, K, Harada, A, Takamisawa, I, Shimokado, K and Kataoka, K (2002). Polyion complex micelles as vectors in gene therapy—pharmacokinetics and *in vivo* gene transfer. *Gene Ther* **9**: 407–414.
9. Jain, RK (2001). Delivery of molecular and cellular medicine to solid tumors. *Adv Drug Deliv Rev* **46**: 149–168.
10. Minchinton, AI and Tannock, IF (2006). Drug penetration in solid tumours. *Nat Rev Cancer* **6**: 583–592.
11. Mellor, HR, Davies, LA, Caspar, H, Pringle, CR, Hyde, SC, Gill, DR *et al.* (2006). Optimising non-viral gene delivery in a tumour spheroid model. *J Gene Med* **8**: 1160–1170.
12. Kanayama, N, Fukushima, S, Nishiyama, N, Itaka, K, Jang, WD, Miyata, K *et al.* (2006). A PEG-based biocompatible block catiomer with high buffering capacity for the construction of polyplex micelles showing efficient gene transfer toward primary cells. *ChemMedChem* **1**: 439–444.
13. Miyata, K, Oba, M, Nakanishi, M, Fukushima, S, Yamasaki, Y, Koyama, H *et al.* (2008). Polyplexes from poly(aspartamide) bearing 1,2-diaminoethane side chains induce pH-selective, endosomal membrane destabilization with amplified transfection and negligible cytotoxicity. *J Am Chem Soc* **130**: 16287–16294.
14. Akagi, D, Oba, M, Koyama, H, Nishiyama, N, Fukushima, S, Miyata, T *et al.* (2007). Biocompatible micellar nanovectors achieve efficient gene transfer to vascular lesions without cytotoxicity and thrombus formation. *Gene Ther* **14**: 1029–1038.
15. Itaka, K, Ohba, S, Miyata, K, Kawaguchi, H, Nakamura, K, Takato, T *et al.* (2007). Bone regeneration by regulated *in vivo* gene transfer using biocompatible polyplex nanomicelles. *Mol Ther* **15**: 1655–1662.
16. Bae, Y, Nishiyama, N, Fukushima, S, Koyama, H, Yasuhiro, M and Kataoka, K (2005). Preparation and biological characterization of polymeric micelle drug carriers with intracellular pH-triggered drug release property: tumor permeability, controlled subcellular drug distribution, and enhanced *in vivo* antitumor efficacy. *Bioconjug Chem* **16**: 122–130.
17. Kano, MR, Bae, Y, Iwata, C, Morishita, Y, Yashiro, M, Oka, M *et al.* (2007). Improvement of cancer-targeting therapy, using nanocarriers for intractable solid tumors by inhibition of TGF-beta signaling. *Proc Natl Acad Sci USA* **104**: 3460–3465.
18. Sutherland, RM (1988). Cell and environment interactions in tumor microregions: the multicell spheroid model. *Science* **240**: 177–184.
19. Han, M, Bae, Y, Nishiyama, N, Miyata, K, Oba, M and Kataoka, K (2007). Transfection study using multicellular tumor spheroids for screening non-viral polymeric gene vectors with low cytotoxicity and high transfection efficiencies. *J Control Release* **121**: 38–48.
20. An, WG, Kanekal, M, Simon, MC, Maltepe, E, Blagosklonny, MV and Neckers, LM (1998). Stabilization of wild-type p53 by hypoxia-inducible factor 1alpha. *Nature* **392**: 405–408.
21. Huang, Y, Leobandung, W, Foss, A and Peppas, NA (2000). Molecular aspects of muco- and bioadhesion: tethered structures and site-specific surfaces. *J Control Release* **65**: 63–71.
22. Samuel, KL, Elizabeth, OD, Harrold, S, Man, ST, Wang, Y, Cone, R *et al.* (2007). Rapid transport of large polymeric nanoparticles in fresh undiluted human mucus. *Proc Natl Acad Sci USA* **104**: 1482–1487.
23. Yoncheva, K, Guembe, L, Campanero, MA and Irache, JM (2007). Evaluation of bioadhesive potential and intestinal transport of pegylated poly(anhydride) nanoparticles. *Int J Pharm* **334**: 156–165.
24. Niwa, H, Yamamura, K and Miyazaki, J (1991). Efficient selection for high-expression transfectants with a novel eukaryotic vector. *Gene* **108**: 193–199.
25. Nagai, T, Ibata, K, Park, ES, Kubota, M, Mikoshiba, K and Miyawaki, A (2002). A variant of yellow fluorescent protein with fast and efficient maturation for cell-biological applications. *Nat Biotechnol* **20**: 87–90.
26. Harada, H, Kizaka-Kondoh, S and Hiraoka, M (2005). Optical imaging of tumor hypoxia and evaluation of efficacy of a hypoxia-targeting drug in living animals. *Mol Imaging* **4**: 182–193.

ARTICLE

Diffuse-Type Gastric Carcinoma: Progression, Angiogenesis, and Transforming Growth Factor β Signaling

Akiyoshi Komuro, Masakazu Yashiro, Caname Iwata, Yasuyuki Morishita, Erik Johansson, Yoshiko Matsumoto, Akira Watanabe, Hiroyuki Aburatani, Hiroyuki Miyoshi, Kunihiko Kiyono, Yo-taro Shirai, Hiroshi I. Suzuki, Kosei Hirakawa, Mitsunobu R. Kano, Kohei Miyazono

Background Diffuse-type gastric carcinoma is a cancer with poor prognosis that has high levels of transforming growth factor β (TGF-β) expression and thick stromal fibrosis. However, the association of TGF-β signaling with diffuse-type gastric carcinoma has not been investigated in detail.

Methods We used a lentiviral infection system to express a dominant-negative TGF-β type II receptor (dnTβRII) or green fluorescent protein (GFP) as a control in the diffuse-type gastric carcinoma cell lines, OCUM-2MLN and OCUM-12. These infected cells and the corresponding parental control cells were subcutaneously or orthotopically injected into nude mice. Angiogenesis was inhibited by infecting cells with a lentivirus carrying the gene for angiogenic inhibitor thrombospondin-1 or by injecting mice intraperitoneally with the small-molecule angiogenic inhibitor sorafenib or with anti-vascular endothelial growth factor (VEGF) neutralizing antibody (six or eight mice per group). Expression of phospho-Smad2 and thrombospondin-1 was investigated immunologically in human gastric carcinoma tissues from 102 patients. All statistical tests were two-sided.

Results Expression of dnTβRII into OCUM-2MLN cells did not affect their proliferation in vitro, but it accelerated the growth of subcutaneously or orthotopically transplanted tumors in vivo (eg, for mean volume of subcutaneous tumors on day 10 relative to that on day 0: dnTβRII tumors = 3.49 and GFP tumors = 2.46, difference = 1.02, 95% confidence interval [CI] = 0.21 to 1.84; $P = .003$). The tumors expressing dnTβRII had higher levels of angiogenesis than those expressing GFP because of decreased thrombospondin-1 production. Similar results were obtained with OCUM-12 cells. Expression of thrombospondin-1 in the dnTβRII tumor or treatment with sorafenib or anti-VEGF antibody reduced tumor growth, whereas knockdown of thrombospondin-1 expression resulted in more accelerated growth of OCUM-2MLN tumors than of GFP tumors (eg, mean tumor volumes on day 14 relative to those on day 0: thrombospondin-1–knockdown tumors = 4.91 and GFP tumors = 3.79, difference = 1.12, 95% CI = 0.80 to 1.44; $P < .001$). Positive association between phosphorylated Smad2 and thrombospondin-1 immunostaining was observed in human gastric carcinoma tissues.

Conclusions Disruption of TGF-β signaling in diffuse-type gastric carcinoma models appeared to accelerate tumor growth, apparently through increased tumor angiogenesis that was induced by decreased expression of thrombospondin-1.

J Natl Cancer Inst 2009;101:592–604

Gastric cancer is one of the most devastating human cancers, with approximately 880 000 new cases and 650 000 deaths worldwide per year (1,2). There are two types of gastric cancer: diffuse type and intestinal type. Diffuse-type gastric carcinoma, according to the Laurén classification (3), is highly metastatic and characterized clinically by rapid disease progression and poor prognosis (4). Although the incidence of intestinal-type gastric carcinoma has continuously decreased, the incidence of diffuse-type gastric carcinoma has increased progressively during the last 30 years, so that

Affiliations of authors: Department of Molecular Pathology and the Global Center of Excellence Program for "Integrative Life Science Based on the Study of Biosignaling Mechanisms," Graduate School of Medicine (AK, CI, YMo, EJ, YMa, KK, Y-tS, HIS, MRK, KM), Center for NanoBio Integration (MRK, KM), and Genome Science Division, Research Center for Advanced Science and Technology (AW, HA), University of Tokyo, Tokyo, Japan; Department of Surgical Oncology, Osaka City University Graduate School of Medicine, Osaka, Japan (MY, KH); Subteam for Manipulation of Cell Fate, Bio Resource Center, RIKEN, Tsukuba, Japan (HM).

Correspondence to: Kohei Miyazono, MD, Department of Molecular Pathology, Graduate School of Medicine, University of Tokyo, Hongo 7-3-1, Bunkyo-ku, Tokyo 113-0033, Japan (e-mail: miyazono-ind@umin.ac.jp).

See "Funding" and "Notes" following "References."

DOI: 10.1093/jnci/djp058

the diffuse type constitutes approximately one-third of all gastric carcinomas diagnosed in the United States (5). In contrast to the intestinal type, infection with *Helicobacter pylori* and chronic gastritis are often absent in the diffuse-type gastric carcinoma. Patients with diffuse-type gastric carcinoma often have thick stromal fibrosis with undifferentiated carcinoma cells scattered in the interstitium, which results in a stiff and thick gastric wall with reduced motility, but the tumors do not form ulcers or apparent mass lesions.

Transforming growth factor β (TGF-β) is a multifunctional cytokine that contributes to cancer progression by acting in both tumor cells and the tumor stroma (6). TGF-β binds to TGF-β serine–threonine kinase receptors type I and type II (TβRII) and transduces signals by phosphorylation of the receptor-regulated Smad2 and Smad3 proteins. Smad2 and Smad3 form complexes with Smad4, and these complexes regulate transcription of various target genes in the nucleus (7,8).

Because TGF-β is a potent inhibitor of epithelial cell proliferation, resistance to the inhibitory activity of TGF-β results in increased cell proliferation and cancer progression (9). Cancer cells in advanced tumors are often refractory to TGF-β–induced growth inhibition, and some tumors even increase their production of TGF-β ligands. TGF-β induces deposition of extracellular matrix in the tumor interstitium, which leads to fibrosis. TGF-β also induces perturbations of immune surveillance and regulates angiogenesis in vivo. Moreover, TGF-β may promote tumor growth by inducing epithelial cells to undergo the epithelial–mesenchymal transition (10,11), and inhibition of TGF-β signaling has been reported to prevent progression and metastasis of certain advanced tumors (12–15). In addition, decreased expression of TβRII, Smad2, and/or Smad4 or loss-of-function mutations in at least one of these genes has been observed in advanced stages of certain cancers, including colorectal cancer, breast cancer, and prostate cancer (16), and these changes in TGF-β signaling may affect progression of these cancers.

There is limited information regarding the role of TGF-β in diffuse-type gastric cancers. The thick stromal fibrosis observed in diffuse-type gastric carcinoma is induced by the TGF-β produced by cancer cells and by cancer-associated fibroblasts (17). Production of TGF-β1 has been reported to be associated with the progression of diffuse-type gastric carcinoma (18), although the relation of TGF-β1 expression to prognosis of gastric carcinoma is controversial (19). Disruption of TGF-β signaling by loss of Smad4 expression has also been observed in diffuse-type gastric carcinoma (20). However, detailed investigations on the roles of TGF-β signaling in diffuse-type gastric carcinoma have not been carried out. We therefore investigated the role of TGF-β signaling in diffuse-type gastric carcinoma by use of OCUM-2MLN and OCUM-12 cell lines and by disrupting TGF-β signaling.

Patients, Materials, and Methods

Cell Lines

The OCUM-2MLN cell line was obtained from a lymph node metastasis of a mouse with orthotopically implantated OCUM-2M cells (21); the OCUM-2M line was originally established from a 49-year-old woman with diffuse-type gastric carcinoma (4). The OCUM-12 cell line was established from the peritoneal effusion of a 58-year-old man with diffuse-type gastric carcinoma that was diagnosed by endoscopy and histology. OCUM-12 cells were further confirmed to be tumorigenic in nude mice [(22) and M. Yashiro and K. Hirakawa, Osaka City University, unpublished data]. Both cell lines were cultured in Dulbecco's modified Eagle medium (DMEM) containing 10% fetal bovine serum, penicillin (100 U/mL), and streptomycin (0.1 mg/mL) (Invitrogen, Carlsbad, CA). To disrupt TGF-β signaling, we introduced a dominant-negative TGF-β type II receptor (dnTβRII) that lacks the intracellular kinase domain into the OCUM-2MLN and OCUM-12 cell lines (resulting in the 2MLN-dnTβRII and OCUM-12-dnTβRII cell lines, respectively) by use of a lentiviral infection system (23). We used the same lentivirus system to generate control OCUM-2MLN and OCUM-12 cells that expressed green fluorescent protein (GFP) (resulting in the 2MLN-GFP and OCUM-12-GFP cell lines, respectively) and OCUM-2MLN cells that expressed both dnTβRII and the angiogenic inhibitor thrombospondin-1 (resulting in the 2MLN-dnTβRII+TSP-1) (24,25). cDNAs for dnTβRII or for thrombospondin-1 were produced from mRNA extracted from the cultured OCUM-2MLN cell line by polymerase chain reaction (PCR). cDNAs encoding either dnTβRII with a carboxyl-terminal hemagglutinin epitope tag or thrombospondin-1 were inserted into the multicloning site of the lentiviral

CONTEXT AND CAVEATS

Prior knowledge

Diffuse-type gastric carcinoma has poor prognosis. Patients have high levels of transforming growth factor β (TGF-β) expression and thick stromal fibrosis.

Study design

The roles of TGF-β and thrombospondin-1, an angiogenic inhibitor that is regulated by TGF-β, were investigated in vitro studies in diffuse-type gastric carcinoma cell lines and in vivo studies in mouse models of diffuse-type gastric carcinoma and human diffuse-type gastric carcinoma tissue specimens from 102 patients.

Contribution

Growth of diffuse-type gastric carcinomas appeared to be accelerated by disruption of TGF-β signaling in mouse models (which may be analogous to what occurs during progression of this disease in humans), apparently because of increased tumor angiogenesis that was induced by decreased expression of thrombospondin-1.

Implications

Because loss of a receptor for TGF-β has been reported to induce tumor angiogenesis in various cancers, administration of angiogenesis inhibitors, such as sorafenib or thrombospondin-1 analogues, should be investigated as a treatment for cancers with disrupted TGF-β signaling pathways.

Limitations

Although mouse models of subcutaneous and orthotopic transplantation models were used, the experiments were conducted with immunocompromised mice. The growth of metastatic tumors was not investigated.

From the Editors

vector pCSII-CMV-RfA by use of pENTR, according to the manufacturer's protocol (Invitrogen).

Antibodies and Reagents

The rabbit polyclonal antibodies against human and mouse phosphorylated Smad2 that were used for immunoblotting were a gift from A. Moustakas and C.-H. Heldin (Ludwig Institute for Cancer Research, Uppsala, Sweden). The rabbit monoclonal antibody against human and mouse phosphorylated Smad2 that was used for immunohistochemistry was from Millipore (Temecula, CA; clone A5S). The rat monoclonal antibody against mouse platelet–endothelial cell adhesion molecule-1 (PECAM-1) and mouse monoclonal antibody against human and mouse Smad2 and Smad3 (clone 18) were from BD (Franklin Lakes, NJ). The rat monoclonal antibody against hemagglutinin tag (clone 3F10) was from Roche (Basel, Swiss), and mouse monoclonal antibody against GFP (clone 1E4) was from Medical & Biological Laboratories, Co. (Woburn, MA). Mouse monoclonal antibody against human and mouse thrombospondin-1 was from Abcam (Cambridge, UK; clone A6.1). Alexa 488– and Alexa 594–conjugated secondary antibodies and the nuclear stain TOTO-3 for counterstaining were from Invitrogen Molecular Probes (Eugene, OR). TGF-β3 and TGF-β1, which show similar biological activities in vitro, were purchased from R&D Systems (Minneapolis, MN).

Immunoblot Analysis

We examined the expression of Smad2 and Smad3, phosphorylated Smad2, GFP, and hemagglutinin-tagged dnTβRII by immunoblot analyses in following cultured cells: 2MLN, 2MLN-GFP, 2MLN-dnTβRII, OCUM-12, OCUM-12-GFP, and OCUM-12-dnTβRII. These cells were lysed in a buffer containing 50 mM Tris–HCl (pH 8.0), 150 mM NaCl, 1% Nonidet P-40 (Nacalai Tesque, Kyoto, Japan), 5 mM EDTA, 0.5% deoxycholic acid sodium salt-monohydrate (Nacalai Tesque), 0.1% sodium dodecyl sulfate (SDS) (Nacalai Tesque), 1% aprotinin (Mitsubishi Pharma, Osaka, Japan), and 1 mM phenylmethylsulfonyl fluoride (Sigma, St Louis, MO). The cell lysates were boiled in SDS sample buffer (100 mM Tris–HCl at pH 8.8, 0.01% bromophenol blue, 36% glycerol, 4% SDS, and 10 mM dithiothreitol) and subjected to SDS–polyacrylamide gel electrophoresis. Proteins were electrotransferred from a polyacrylamide gel to Pall Fluorotrans-W membranes (Pall, East Hills, NY) and immunoblotted with antibodies. Bound antibodies were detected by use of an enhanced chemiluminescence detection system (Amersham Pharmacia Biotech, Piscataway, NJ). Each experiment was conducted two times, and a representative result is shown.

Cell Proliferation Assay

We cultured 2.5×10^4 2MLN, 2MLN-GFP, 2MLN-dnTβRII, or OCUM-12 cells per well in 12-well plates. On the next day (designated as day 0), some cultures were treated with TGF-β and control cultures were left untreated. Cells from duplicate cultures were counted as indicated with a hemocytometer. Each experiment was conducted two times, sample points were assayed in triplicate, and data were averaged. Data from one representative experiment of these are shown.

BALB/c Nude Mouse Model for Human Gastric Cancer

BALB/c nude male mice, aged 4–5 weeks, were obtained from Oriental Yeast Co. (Tokyo, Japan). All animal experimental protocols were performed in accordance with the policies of the Animal Ethics Committee of the University of Tokyo. A total of 5×10^6 cells in 100 μL of DMEM (n > 6 mice per group) was injected subcutaneously at the left flank of each mouse and allowed to grow for 1 week (for OCUM-2MLN cells) or 3 weeks (for OCUM-12 cells) when the major axis of the tumors was approximately 10 mm long. For the orthotopic transplantation model, a total of 5×10^6 cells in 50 μL of DMEM were injected into the gastric wall of each mouse (n = 8 mice per group) and allowed to grow for 1 week when tumor was approximately 5 mm in diameter.

Tumor Volume Measurement

The volume of subcutaneous xenograft tumors was measured externally every other day until the end of the evaluation period. Tumor volume was estimated by using the equation, $v = (ab^2)/2$, where v is volume, a is the length of the major axis of the tumor, and b is the length of its minor axis. The relative tumor volume was then calculated by dividing tumor volume on a given experimental day by that on day 0 (the day of initiation of treatment or evaluation). For orthotopic xenograft tumors, the tumor area on the gastric wall was measured by opening the abdomen on experimental day 14 and at the end of the evaluation period (day 21). The major and minor axes of tumors were measured with Adobe Photoshop software (Adobe Systems, Mountain View, CA), and tumor areas on the gastric wall were calculated with ImageJ software (National Institutes of Health, Bethesda, MD). Relative tumor area was obtained by dividing the area on day 21 by that on day 14.

RNA Isolation and Quantitative Real-Time Reverse Transcription-PCR

Total RNAs from gastric carcinoma cells or excised subcutaneous tumors were extracted with the RNeasy Mini Kit (QIAGEN, Valencia, CA). Sources of RNAs were as follows: cultured 2MLN, 2MLN-GFP, and 2MLN-dnTβRII cells at 0, 1, and 24 hours treated with TGF-β ligand at 1 ng/mL or left untreated (*see* Figure 1, B); cultured 2MLN-GFP and 2MLN-dnTβRII cells at 24 hours treated with TGF-β ligand at 1 ng/mL or left untreated, and subcutaneous tumors generated from these cells that were allowed to grow for 3 weeks in vivo (*see* Figure 2); cultured 2MLN-GFP, 2MLN-GFP+miTSP-1, and 2MLN-dnTβRII cells treated with TGF-β ligand at 1 ng/mL or left untreated, and subcutaneous tumors generated from these cells in vivo that were allowed to grow for 3 weeks (*see* Figure 4); and cultured OCUM-12-GFP and OCUM-12-dnTβRII cells at 24 hours treated with TGF-β ligand at 1 ng/mL or left untreated (*see* Figure 5). First-strand cDNAs were synthesized with the Quantitect Reverse Transcription kit (QIAGEN) with random hexamer primers. Quantitative real-time reverse transcription (RT)-PCR analysis was performed with the 7500 Fast Real-Time PCR system (Applied Biosystems, Foster City, CA) with the primers, as shown in Supplementary Table 1 (available online). Each experiment was conducted two times, each sample was assayed in triplicate, and data were averaged. Data from one representative experiment are shown.

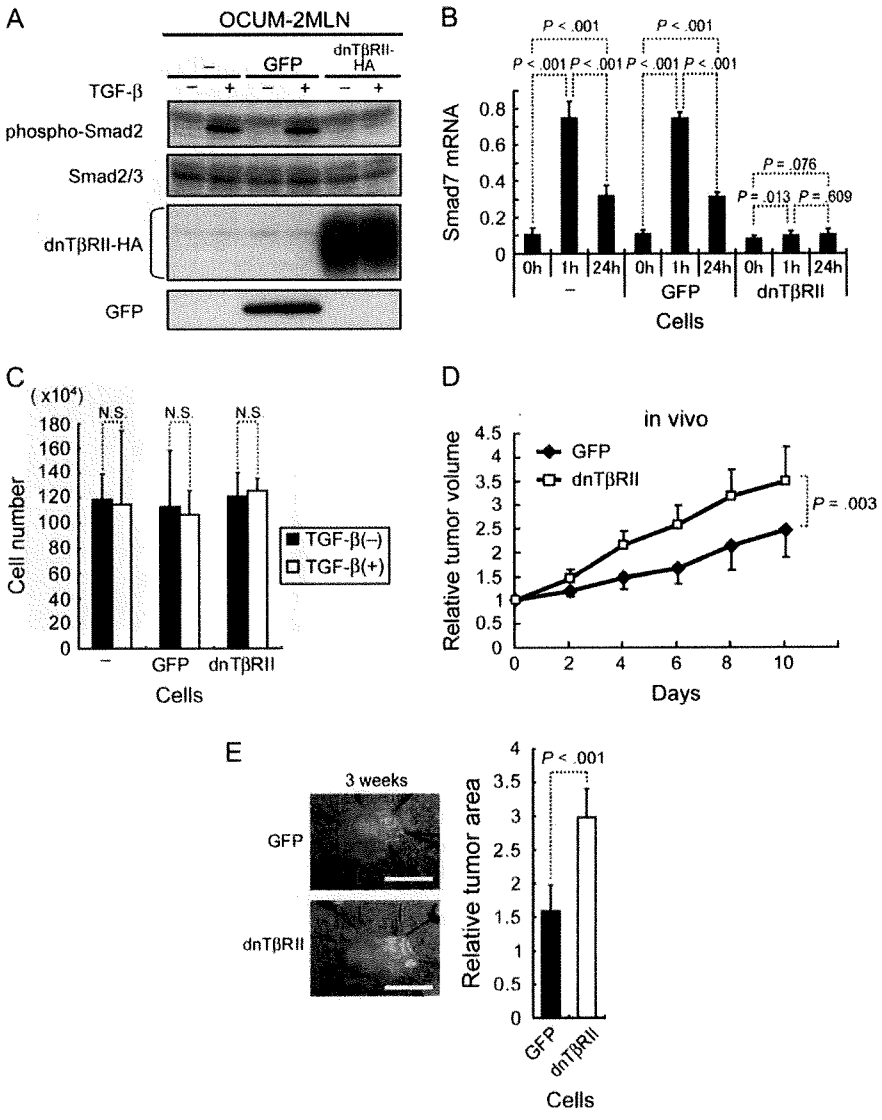

Figure 1. Disruption of TGF-β in gastric cancer cells and tumors. We used parental OCUM-2MLN cells, 2MLN cells expressing GFP (termed 2MLN-GFP cells) as a control, and 2MLN cells expressing a dnTβRII (termed 2MLN-dnTβRII cells). **A)** TGF-β signal transduction in the cells. Immunoblot analysis was used to compare the level of phosphorylated Smad2 (phospho-Smad2) with that of Smad2 and 3 as control, in parental OCUM-2MLN cells (**lanes** – = cells carry no constructs), 2MLN-GFP cells (**lanes GFP**), and 2MLN-dnTβRII cells (**lanes dnTβRII**), treated with TGF-β3 (1 ng/mL) or left untreated for 1 hour. Expression of dnTβRII protein (by use of hemagglutinin [HA] tag), and that of GFP, as a control for lentiviral infection was also determined by immunoblot analysis. The cells were subjected to immunoblot analysis with antibodies against the proteins indicated to the **left**. The experiment was conducted two times, and data from one representative experiment are shown. **B)** Human Smad7 mRNA expression. Quantitative real-time polymerase chain reaction was used to assess the level of expression of human Smad7 mRNA in all three cell lines after treatment with TGF-β3 (1 ng/mL), as indicated. The experiment was conducted two times, each sample was assessed in triplicate, and data were averaged. Data from one representative experiment are shown. **C)** Proliferation of gastric cancer cells in the presence of TGF-β3. Cells were treated with TGF-β3 (1 ng/mL) in 10% fetal bovine serum for 3 days; control cells were not treated with TGF-β3. The experiment was conducted two times, each sample was assessed in triplicate, and data were averaged. Data from one representative experiment are shown. **D)** Growth of 2MLN-GFP and 2MLN-dnTβRII tumors in nude mice for 10 days. Cells were subcutaneously transplanted into nude mice (n = 8 mice per group). **E)** Growth of orthotopic 2MLN-GFP and 2MLN-dnTβRII tumors in nude mice. Cells were transplanted into the gastric wall of nude mice (n = 8 mice per group). **Left)** Macroscopic appearance of representative samples of excised gastric wall with an orthotopic tumor. **Right)** Relative areas of the 2MLN-GFP and 2MLN-dnTβRII tumors. Scale bar = 10 mm. **Error bars** = 95% confidence intervals. All *P* values (two-sided) were calculated by using a Student's *t* test, except for that in (**D**), which was calculated by using a two-way repeated measures analysis of variance. dnTβRII = dominant-negative TGF-β type II receptor; GFP = green fluorescent protein; TGF-β = transforming growth factor β.

Microarray Analysis of Gene Expression in 2MLN-GFP or 2MLN-dnTβRII Tumors

Tissue samples from subcutaneous 2MLN-GFP or 2MLN-dnTβRII tumors were digested with collagenase (Worthington, Lakewood, NJ; 1 mg/mL) at 37°C for 1 hour, followed by treatment with 0.25% trypsin–EDTA (Invitrogen) at 37°C for 15 minutes. The resulting single-cell suspension was subjected to magnetic cell sorting (MACS®) with magnetic microbeads conjugated to CD326 antibody (Miltenyi Biotec, Auburn, CA) to separate CD326-positive human cancer cells from CD326-negative mouse stromal cells. Total RNAs from the isolated cancer cells were purified with the RNeasy Mini Kit (QIAGEN) and used for microarray analysis. Biotin-labeled complementary RNAs were synthesized and hybridized to the oligonucleotide microarray, GeneChip Human Genome U133 Plus2.0 (Affymetrix, Santa Clara, CA), according to Affymetrix technical manual. Gene expression data were normalized by use of the MAS5 algorithm according to the manufacturer's instruction. DAVID functional annotation clustering (26) with the Kyoto Encyclopedia of Genes and Genomes pathway database (http://genome.ad.jp/kegg/) was used for pathway analysis of the top 50 most variable probe sets of the GeneChip.

Histochemistry and Immunohistochemistry in Mouse Tissues

Excised mouse tissue samples were fixed for 1 hour in 10% neutral-buffered formalin at room temperature, washed overnight in phosphate-buffered saline containing 10% sucrose at 4°C, and embedded in optimal cutting temperature compound (Tissue-Tek; Sakura Finetek, Tokyo, Japan). Some samples were then snap frozen in a dry ice–acetone bath for immunohistochemistry, and other samples were fixed overnight in 4% paraformaldehyde and then embedded in paraffin for hematoxylin–eosin staining or AZAN staining to visualize collagen fibers. Frozen samples were

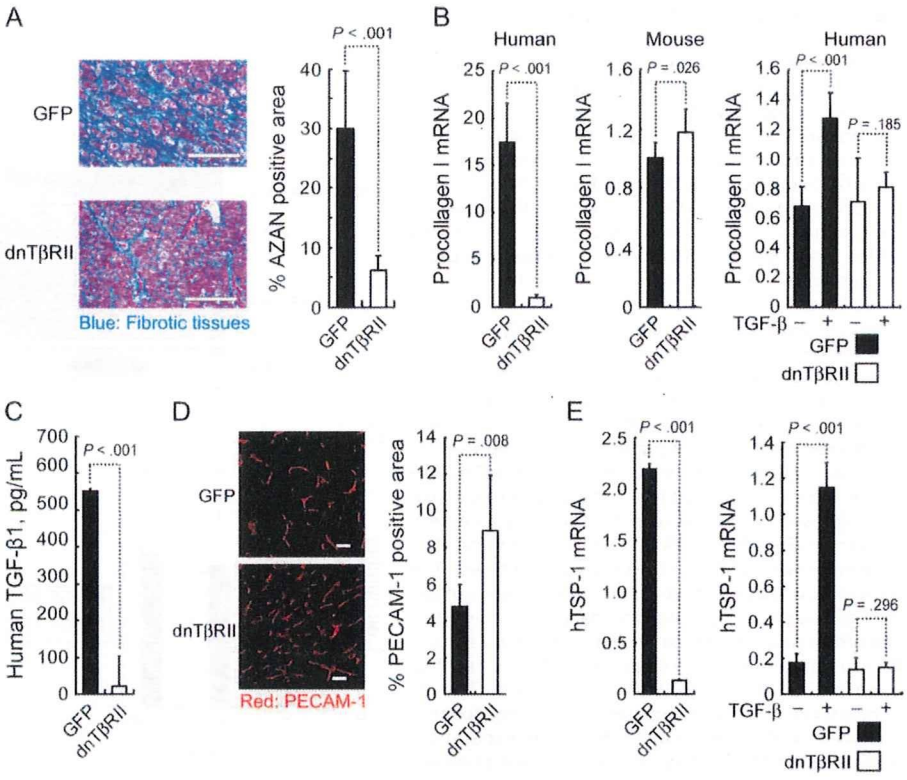

Figure 2. Histological characterization of 2MLN-GFP and 2MLN-dnTβRII xenograft tumors from nude mice. **A)** Fibrotic tissue in subcutaneous 2MLN-GFP (GFP) or 2MLN-dnTβRII (dnTβRII) xenograft tumors. **Left)** On day 14, fibrotic areas of tumor sections were visualized by AZAN staining and examined via light microscopy. Scale bars = 100 μm. **Right)** Quantification of fibrotic areas (n = 9 with each condition). **B)** Expression of human and mouse procollagen I mRNAs. **Left)** 2MLN-GFP subcutaneous tumors in nude mice. **Middle)** 2MLN-dnTβRII subcutaneous tumors in nude mice. **Right)** TGF-β treatment in 2MLN-GFP and 2MLN-dnTβRII cell lines. Cells were treated with TGF-β for 24 hours or left untreated (as indicated) and assayed for procollagen I mRNA with quantitative real-time polymerase chain reaction. Each experiment was conducted two times, each sample was assessed in triplicate, and data were averaged. Data from one representative experiment of these are shown. **C)** Concentrations of human TGF-β1 protein in 2MLN-GFP and 2MLN-dnTβRII cell culture supernatants. The level of TGF-β1 protein was determined by an enzyme-linked immunosorbent assay with an antibody specific for TGF-β1. The experiment was conducted two times, each sample was assessed in triplicate, and data were averaged. Data from one representative experiment of these are shown. **D)** Vascular density in 2MLN-GFP and 2MLN-dnTβRII xenograft tumors. Vascular density was determined by immunostaining with an antibody against PECAM-1 (n = 6 mice per group). **Left)** Micrographs of immunostained 2MLN-GFP and 2MLN-dnTβRII xenograft tumor sections. PECAM-1–positive areas are shown in **red** (n = 6 with each condition). Scale bars = 100 μm. **Right)** Percent PECAM-1–positive areas in 2MLN-GFP and 2MLN-dnTβRII xenograft tumor sections per microscopic field (n = 6 with each condition). **E)** Expression of hTSP-1 mRNA. **Left)** 2MLN-GFP and 2MLN-dnTβRII tumors in nude mice. **Right)** 2MLN-GFP and 2MLN-dnTβRII cells treated with TGF-β or left untreated for 24 hours in vitro, as indicated. Each experiment was conducted two times, each sample was assessed in triplicate, and data were averaged. Data from one representative experiment are shown. **Error bars** = 95% confidence intervals. All *P* values (two-sided) were calculated with a Student's *t* test. dnTβRII = dominant-negative TGF-β type II receptor; GFP = green fluorescent protein; TGF-β = transforming growth factor β; hTSP-1 = human thrombospondin-1; PECAM-1 = platelet–endothelial cell adhesion molecule-1.

further sectioned at a thickness of 10 μm with a cryostat, briefly fixed with 10% formalin, and then incubated with primary and secondary antibodies. Formalin-fixed samples of subcutaneous tumors and orthotopic tumors were subjected to hematoxylin–eosin and AZAN staining (*see* Figures 2, A and 4, C and Supplementary Figure 1, A, available online). Frozen samples of subcutaneous tumors were immunostained with anti-PECAM-1 and anti-rat Alexa 594 antibodies (*see* Figures 2, D and 4, B), or with anti-hemagglutinin and anti-rat Alexa 594 antibodies with TOTO-3 nuclear stain (*see* Figure 3, B). Frozen samples of orthotopic tumors were immunostained with anti-PECAM-1 and anti-rat Alexa 594 antibody (Supplementary Figure 1, B, available online).

Enzyme-Linked Immunosorbent Assay

Production of TGF-β1 by 2MLN-GFP and 2MLN-dnTβRII cells was determined with a sandwich enzyme immunoassay technique by using a Quantikine human TGF-β1 immunoassay (R&D Systems), according to the manufacturer's instruction. A total of 1×10^6 cells were cultured in 1% fetal bovine serum in six-well plates for 24 hours, and 100 μL of conditioned medium was removed and treated with 20 μL of 1 M HCl for 10 minutes, followed by neutralization with 20 μL of 1.2 M NaOH in 0.5 M HEPES (pH 7.4). Without this acidification step with 1 M HCl, levels of TGF-β1 in the conditioned medium could not be detected by the enzyme-linked immunosorbent assay. The samples were then pipetted into the wells of the microplate that had been precoated with a monoclonal antibody specific for TGF-β1 and incubated for 2 hours at room temperature. Subsequently, an enzyme-linked polyclonal antibody specific for TGF-β1 was added to the wells and incubated for additional 2 hours at room temperature to sandwich the TGF-β1 ligand. After a wash to remove unbound antibody–enzyme reagent, a substrate solution consisting of hydrogen peroxide and tetramethylbenzidine was added to the wells, and the intensity of the color developed was determined with a microplate reader (BIO-RAD, Hercules, CA). Each experiment was conducted two times, each sample point was assessed in triplicate, and data were averaged. Data from one representative experiment are shown.

Reduction of Thrombospondin-1 Expression by Use of MicroRNAs

The Block-iT Pol II miR RNAi expression system (Invitrogen) was used to knockdown the expression of thrombospondin-1. A microRNA construct against thrombospondin-1 was cloned into the pcDNA6.2-GW/EmGFP-mir vector (Invitrogen) after annealing the oligonucleotide 5′-AGAACTCAGTTACCATCTGCA-3′, which was designed to knockdown the expression of thrombospondin-1 by using BLOCK-iT RNAi Designer (Invitrogen). The EmGFP-miR thrombospondin-1 expression site was then inserted

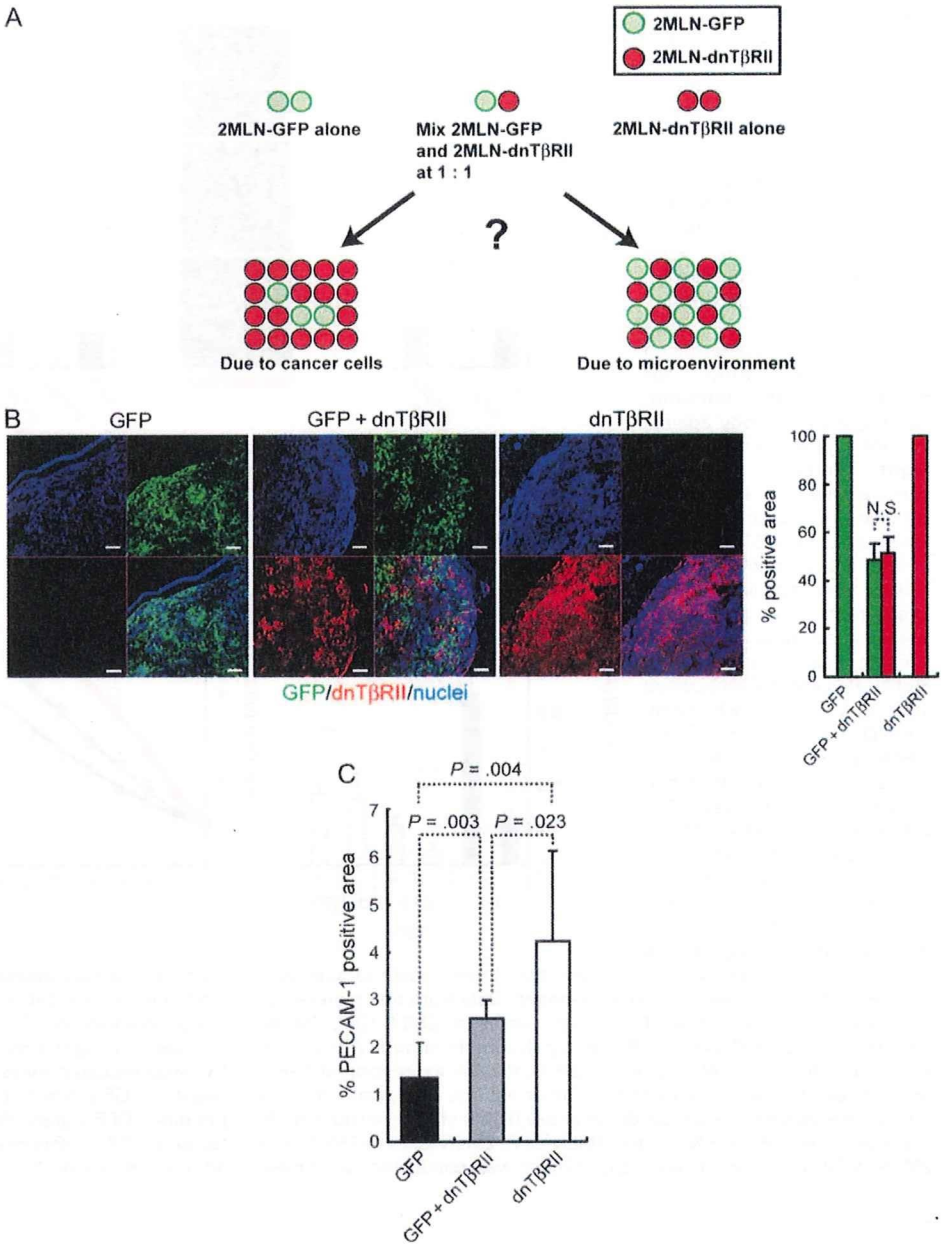

Figure 3. Characterization of xenograft tumors with a mixture of equal numbers of 2MLN-GFP (GFP) and 2MLN-dnTβRII (dnTβRII) cells. **A)** Developmental model of tumors inoculated with a mixture of 2MLN-GFP and 2MLN-dnTβRII. Equal amounts of the 2MLN-GFP and 2MLN-dnTβRII cells were mixed and transplanted into nude mice. The composition of tumors generated with a mixture of 2MLN-GFP and 2MLN-dnTβRII cells was compared with that of tumors generated with 2MLN-GFP or 2MLN-dnTβRII cells alone to investigate whether the tumor microenvironment serves as a major determinant of tumor growth. **B)** Distribution of 2MLN-GFP cells (GFP, **green**) and 2MLN-dnTβRII cells (as shown by a hemagglutinin tag that was detected with anti-hemagglutinin antibody, **red**) in mixed-cell tumors. 2MLN-GFP cells were identified by GFP fluorescence, and 2MLN-dnTβRII cells were identified by immunohistochemistry staining with an antibody specific for hemagglutinin and with nuclear counterstaining with TOTO-3. **Left)** Micrographs of sections from tumors generated with 2MLN-GFP cells alone, 2MLN-dnTβRII cells alone, or a mixture of both cell lines. Scale bars = 100 μm. **Right)** Percent hemagglutinin-positive areas and GFP-positive areas (n = 9 with each condition). **C)** Vascular areas in tumors generated with 2MLN-GFP cells alone, 2MLN-dnTβRII cells alone, or a mixture of both cell types. Vascular areas were identified by immunostaining with antibody against PECAM-1 (n = 3 in each condition). **Error bars** = 95% confidence intervals. All *P* values (two-sided) were calculated using the Student's *t* test. dnTβRII = dominant-negative TGF-β type II receptor; GFP = green fluorescent protein; TGF-β = transforming growth factor β; PECAM-1 = platelet–endothelial cell adhesion molecule-1.

into the pDONR221 vector (Invitrogen) by the BP recombination reaction according to the manufacturer's instructions, followed by its insertion into multicloning site of the lentiviral vector pCSII-EF-MCS LR recombination reaction (Invitrogen), according to the manufacturer's instruction. Stably transfected 2MLN-GFP cells, termed 2MLN-GFP+miTSP-1, in which the expression of thrombospondin-1 was silenced, were established by use of the lentiviral infection system by the methods as described above (23).

Treatment With Angiogenesis Inhibitors In Vivo

A small-molecule inhibitor of angiogenesis, sorafenib (Nexavar; Bayer Health Care, Leverkusen, Germany), was dissolved at 10 mg/mL in dimethyl sulfoxide as stock solution (ie, 5 mL of dimethyl sulfoxide was added to one-fourth of a 200-mg sorafenib tablet). An 80-μL aliquot of the sorafenib stock solution (800 μg of sorafenib) was diluted with 170 μL of phosphate-buffered saline to a final concentration of 3.2 mg/mL. One week after subcutaneous transplantation with 2MLN-GFP or 2MLN-dnTβRII cells or 4 weeks after subcutaneous transplantation with OCUM-12-GFP and OCUM-12-dnTβRII cells (n = 6 mice per group), sorafenib or a vehicle control was administered intraperitoneally to BALB/c nude mice every day. Fifty micrograms of anti-vascular endothelial growth factor (VEGF) neutralizing monoclonal antibody (MAB293; R&D Systems) (2.5 mg/kg) dissolved in 250 μL of phosphate-buffered saline to a concentration of 0.2 mg/mL or vehicle was intraperitoneally injected into these nude mice (n = 6 mice per group) twice a week for 14 days.

Immunohistochemistry of Human Gastric Cancer Tissues

We examined 102 consecutive surgical samples from patients with gastric cancer at the Osaka City University Hospital, Osaka, Japan,

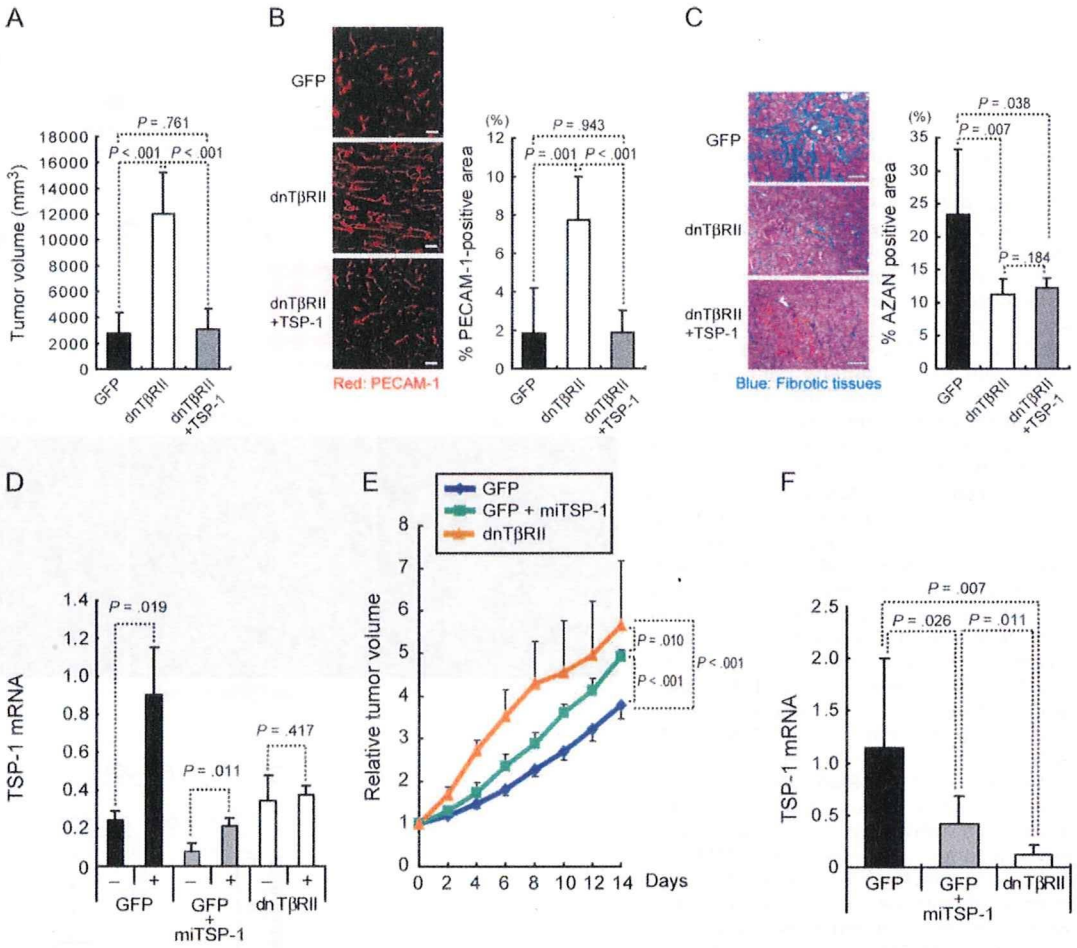

Figure 4. Expression of TSP-1 and tumor growth in nude mice. **A**) Tumor volume and TSP-1 expression. The 2MLN-dnTβRII cells, which stably express TSP-1, are termed 2MLN-dnTβRII+TSP-1. Volumes of the subcutaneous tumors produced by 2MLN-GFP, 2MLN-dnTβRII, and 2MLN-dnTβRII+TSP-1 cells were determined 7 days after inoculation (n = 6 mice per group). **B**) Vascular density at 7 days after inoculation as determined by immunostaining for PECAM-1. **Left**) Immunostaining with antibody against PECAM-1. Scale bars = 100 μm. **Right**) Percent PECAM-1–positive area (n = 3 with each condition). **C**) Fibrotic tissue as determined by AZAN staining in the subcutaneous tumors 7 days after inoculation. **Left**) Micrographs with fibrotic tissue stained **blue** by AZAN staining. Scale bars = 100 μm. **Right**) Percent AZAN-positive area (n = 3 with each condition). **D**) The effect of miTSP-1 mRNA expression in the gastric cancer cells as determined by TSP-1 mRNA expression. The 2MLN-GFP, 2MLN-GFP+miTSP-1, and 2MLN-dnTβRII cells were treated with TGF-β or left untreated for 24 hours in vitro, and expression of TSP-1 mRNA was compared among the cell lines. The experiment was conducted two times, each sample was assayed in triplicate, and data were averaged. Data from one representative experiment are shown. **E**) Growth curves of 2MLN-GFP, 2MLN-GFP+miTSP-1, and 2MLN-dnTβRII xenograft tumors in nude mice (n = 6 in each condition). In 2MLN-GFP+miTSP-1 cells, the expression of TSP-1 was reduced by use of the miTSP-1. Tumor volume is shown relative to the average volume in each condition at day 0 after starting evaluation. **F**) Expression of TSP-1 mRNA in the 2MLN-GFP, 2MLN-GFP+miTSP-1, and 2MLN-dnTβRII tumors in vivo. Experiment was conducted two times, each sample was assessed in triplicate, and data were averaged. Data from one representative experiment are shown. **Error bars** = 95% confidence intervals. All *P* values (two-sided), except for those in (**E**), were calculated using the Student's *t* test. *P* values in (**E**) were calculated by two-way repeated measures analysis of variance. dnTβRII = dominant-negative TGF-β type II receptor; miTSP-1 = microRNA against thrombospondin-1; GFP = green fluorescent protein; TGF-β = transforming growth factor β; TSP-1 = thrombospondin-1; PECAM-1 = platelet–endothelial cell adhesion molecule-1.

which were obtained under a blanket written informed consent. Tissue sections were prepared from paraffin blocks and then incubated in antigen retrieval solution (Histo VT one; Nacalai Tesque, Kyoto, Japan) at 105°C for 20 minutes for thrombospondin-1 and for 40 minutes for phosphorylated Smad2. Sections were immunostained with primary and secondary antibodies. The primary antibodies used were rabbit anti-phosphorylated Smad2 monoclonal antibody and mouse anti-thrombospondin-1 monoclonal antibody. Secondary antibodies used were Alexa 488–conjugated goat anti-rabbit IgG antibody and/or Alexa 594–conjugated goat anti-mouse IgG antibody and were visualized by use of a Zeiss LSM510 Meta confocal microscope (Thornwood, NY) for immunohistochemistry and GFP fluorescence, and with an Olympus (Tokyo, Japan) AX80 microscope for hematoxylin–eosin and AZAN staining. Sections were scored positive when more than approximately 10% of the cancer cells were moderately or strongly stained, according to a recent study (27). In control experiments, the primary antibodies were omitted.

Statistical Analyses

Results were analyzed statistically by two-sided Student's *t* tests or by two-way repeated measures analysis of variance (ANOVA) tests with JMP6 software (SAS Institute, Raleigh, NC), where applicable. Results of immunohistochemistry for human surgical samples were analyzed with the χ^2 test. Results were considered to be statistically significant at $P < .05$. All statistical tests were two-sided.

Results

Disruption of TGF-β Signaling and Growth of Xenografted Tumors in Mice

We investigated the role of TGF-β signaling in human diffuse-type gastric carcinoma by transfecting OCUM-2MLN cells with lentiviral constructs expressing dnTβRIIs or a GFP control. We first determined whether the parental OCUM-2MLN cells and transfected 2MLN-GFP and 2MLN-dnTβRII cells respond to TGF-β in vitro by expressing GFP or dnTβRII, by use of